1 **Integrating field, textural and geochemical monitoring to track eruption triggers and**

2 **dynamics: a case-study from Piton de la Fournaise**

3

4 Lucia Gurioli[1], Andrea Di Muro[2], Ivan Vlastélic[1], Séverine Moune[1], Simon Thivet[1],

5 Marina Valer[1], Nicolas Villeneuve[2], Guillaume Boudoire[2,3], Aline Peltier[2], Patrick

6 Bachèlery[1], Valerie Ferrazzini[2], Nicole Métrich[2], Mhammed Benbakkar[1], Nicolas

7 Cluzel[1], Christophe Constantin[1], Jean-Luc Devidal[1], Claire Fonquernie[1], Jean-Marc

8 Hénot[1]

9 (1) Université Clermont Auvergne, CNRS, IRD, OPGC, Laboratoire Magmas et Volcans, F-63000

10 Clermont-Ferrand, France

11 (2) Institut de Physique du Globe (IPGP), Sorbonne Paris-Cite, CNRS UMR-7154, Université Paris

12 Diderot, Observatoire Volcanologique du Piton de la Fournaise (OVPF), Bourg Murat, France,

13 (3) Laboratoire Géosciences Réunion, Université de La Réunion, Institut de Physique du Globe de

14 Paris, Sorbonne Paris-Cité, UMR 7154 CNRS, F-97715 Saint-Denis, France

15 Corresponding author: L Gurioli, Université Clermont Auvergne, CNRS, IRD, OPGC, LMV

16 Campus Universitaire des Cézeaux, 6 Avenue Blaise Pascal, 63178 Aubière Cedex

17 (lucia.gurioli@uca.fr)

18

19 **Abstract**

20 The 2014 eruption at Piton de la Fournaise (PdF), La Réunion, which occurred after 41

21 months of quiescence, began with surprisingly little precursory activity, and was one of the

22 smallest so far observed at PdF in terms of duration (less than 2 days) and volume (less than

23 0.4×10^6 m^3). The pyroclastic material was composed of golden basaltic pumice along with

24 fluidal, spiny-iridescent and spiny-opaque basaltic scoria. Density analyses performed on 200

25 lapilli reveal that the spiny-opaque clasts are the densest (1600 kg/m^3) and richest in crystals

26 (55 vol. %), and the golden pumices are the least dense (400 kg/m^3) and poorest in crystals (8

27 vol. %). The connectivity data indicate that the fluidal and golden (Hawaiian-like) clasts have

28 more isolated vesicles (up to 40 vol. %) than the spiny (Strombolian-like) clasts (0-5 vol. %).

29 These textural variations are linked to primary pre-eruptive magma storage conditions. The

30 golden and fluidal fragments track the hotter portion of the melt, in contrast to the spiny

31 fragments and lava that mirror the cooler portion of the shallow reservoir. Exponential

32 decrease of the magma ascent and output rates corresponded to progressive tapping of these

distinct portions of the storage system. Increasing syn-eruptive degassing and melt-gas decoupling led to a decrease in the explosive intensity from early fountaining to Strombolian activity. The geochemical results confirm the absence of new hot input of magma into the 2014 reservoir and confirm the emission of a single, shallow, differentiated magma source, possibly related to residual magma from the November 2009 eruption. Fast volatile exsolution and crystal-melt separation (second boiling) were triggered by deep pre-eruptive magma transfer and stress field change. Our study highlights the possibility that shallow magma pockets can be quickly reactivated by deep processes without mass or energy (heat) transfer and produce hazardous eruptions with only short term elusive precursors.

Key words: Piton de la Fournaise, Hawaiian activity, Strombolian activity, shallow reservoire, texture, petrology, geochemistry

1. Introduction

A detailed characterization and understanding of eruptive dynamics and of processes driving and modulating volcano unrest is crucial in monitoring active volcanoes and fundamental for forecasting volcanic eruptions (Sparks, 2003). Many studies suggest that eruptive phenomena are strongly dependent on the physico-chemical properties of ascending magma in the conduit (e.g., temperature, viscosity, porosity, and permeability) (e.g. Sparks, 1978; Rust and Cashman, 2011; Gonnermann and Manga, 2013; Polacci et al., 2014). Integrating petrographic, chemical and textural data can thus provide critical information to constrain both the pre-eruptive storage conditions, and the processes related to magma ascent, degassing and cooling (e.g., reference in Table 1 in Gurioli et al., 2015). This multidisciplinary approach is of even greater importance in the monitoring of volcanoes which emit relatively uniform magma compositions over time, like basaltic volcanoes (e.g. Di Muro et al., 2014; Gurioli et al., 2015; Coppola et al., 2017). As a result, monitoring of textures, and petrochemical properties of lava fragments and pyroclasts is now routinely carried out on a daily basis at active volcanoes such as Kilauea, Etna, and Stromboli (e.g., Taddeucci et al., 2002; Thornber et al., 2003; Polacci et al., 2006; Swanson et al., 2009; Colo' et al., 2010; Houghton et al., 2011; 2013; 2016; Carey et al., 2012; 2013; Lautze et al., 2012; Andronico et al., 2013a; b; 2014; Corsaro and and Miraglia, 2014; Di Muro et al., 2014; Gurioli et al.; 2014; Eychenne et al., 2015; Leduc et al., 2015; Kahl et al., 2015). In the past, time series of petrographic and geochemical data have been measured for PdF basalts and particularly for effusive products. The aim of these datasets was to constrain the spatial and temporal evolution of magma for

65   one of the most active basaltic volcanoes of the world (e.g. Albarède et al., 1997; Vlastélic et

66   al., 2005; 2007, 2009; Boivin and Bachèlery, 2009; Peltier et al., 2009; Schiano et al., 2012;

67   Lénat et al., 2012; Di Muro et al., 2014; 2015; Vlastèlic and Pietruszka, 2016). However, this

68   type of approach has seldom been coupled with detailed textural studies at PdF and instead

69   has mostly focused on crystal textures and crystal size distribution (Welsch et al., 2009; 2013;

70   Di Muro et al., 2014; 2015). Moreover, only sporadic data exist on the textures of pyroclasts

71   ejected by the eruptions at PdF (Villemant et al., 2009; Famin et al., 2009; Welsch et al., 2009;

72   2013; Michon et al., 2013; Vlastélic et al., 2013; Di Muro et al., 2015; Morandi et al., 2016;

73   Ort et al., 2016).

74   Within this paper, we present a multidisciplinary textural, chemical and petrological

75   approach to quantify and understand the short-lived 2014 PdF eruption. This approach

76   combines detailed study of the pyroclastic deposit (grain size and componentry) with bulk

77   texture analysis (density, vesicularity, connectivity, permeability, morphology, vesicle

78   distribution and crystal content) and a petro-chemical study (bulk rock, glass, minerals, melt

79   inclusions) of the same clasts. This integrated approach has now been formalized within the

80   French National Observation Service for Volcanology (SNOV), as routine observational

81   systems   (DynVolc),   Dynamics   of   Volcanoes,   (http://wwwobs.univ-

82   bpclermont.fr/SO/televolc/dynvolc/) and GazVolc, Observation des gaz volcaniques,

83   (http://wwwobs.univ-bpclermont.fr/SO/televolc/gazvolc) to provide data for the on-going

84   activity at PdF (Harris et al., 2017).

85   In spite of being the first of a series of eruptions, the June 2014 event was preceded by

86   only weak inflation and by a rapid increase in number of shallow (< 2 km below volcano

87   summit) volcano tectonic earthquakes that happened only 11 days before the eruption (Peltier

88   et al., 2016). The eruptive event was dominantly effusive, lasted only 20 hours and emitted a

89   very small volume of magma (ca. 0.4 x 10^6 m^3, Peltier et al., 2016), which makes this event

90   one of the smallest, in terms of duration and volume, observed at PdF up to now. In addition,

91   the eruption started during the night and very little direct observation exists for the first few

92   hours of the activity, when the lava effusion was associated with very weak fountaining

93   activity and Strombolian explosions.

94   This eruption occurred just outside the southern border of the summit Dolomieu

95   caldera, at the top of the central cone of PdF (Fig. 1). This is a high risk sector because of the

96   high number of tourists. Identification of precursors of this kind of activity represents an

97   important challenge for monitoring systems (Bachélery et al., 2016).

98   Therefore this eruption represents an ideal context to apply our multidisciplinary

3

99   approach, with the aim of addressing the following key questions:

100   (i)   why was such a small volume of magma erupted instead of remaining

101   endogenic?

102   (ii)   what caused the rapid trigger and the sudden end to this small volume

103   eruption?

104   (iii)   which was the source of the eruption (shallow versus deep, single versus

105   multiple small magma batches)?

106   (iv)   what was the ascent and degassing history of the magma?

107   (v)   what was the time and space evolution of the eruptive event?

108   Furthermore, this eruption provides an exceptional opportunity to study processes leading to

109   the transition from mild Hawaiian (<20 m high fountains, following the nomenclature

110   proposed by Stovall et al., 2011) to Strombolian activity (<10 m high explosions), whose

111   products are little modified by post-fragmentation processes because of the very low intensity

112   of the activity.

2 The 2014 activity

113

2.1 Precursory activity

114

115   The 20 June 2014 summit eruption represents the first eruption at PdF after 41 months of

116   quiescence. The last eruption had been on 9 December 2010, with a shallow (above sea level)

117   intrusion on 2 February 2011 (Roult et al., 2012). From 2011, the deformation at PdF was

118   constant with two distinct types of behaviour: (i) a summit contraction of a few centimetres

119   every year (Fig. 1d), and (ii) a preferential displacement of the east flank at a rate of 1-3

120   centimetres per year (Brenguier et al., 2012; Staudacher and Peltier, 2015). The background

121   microseismicity was very low (< 5 shallow events/day below volcano summit) and low-

122   temperature summit intracaldera fumaroles emitted very little sulphur (H_2S or SO_2) and

123   carbon (CO_2) (Di Muro et al., 2016). After 41 months of rest, a new intense cycle of activity

124   (June 2014, February 2015, May 2015, July 2015, August-October 2015; May 2016;

125   September 2016; January 2017 and July 2017) began with surprisingly little and ambiguous

126   precursory activity.

127   The 2014 summit eruption started during the night of June 20/21, at 21h35 GMT

128   (0h35 local time) and ended on June 21 at 17h09 GMT (21h09 local time), after less than 20

129   hours of dominantly effusive activity. The volcano reawakening was preceded, in March and

130   April 2014, by deep (15-20 km below sea level) eccentric seismicity and increase in soil CO_2

4

131 flux below the western volcano flank, 15 km NW of the volcano summit (Liuzzo et al., 2015;
132 Boudoire et al., 2017). Background micro-seismicity and inflation of the central cone
133 increased progressively starting on 9 June 2014. Weak inflation recorded on both distal and
134 summit baselines (Fig. 1d) suggest that deep (below sea level) magma up-rise was
135 pressurizing the shallow (above sea level) magma storage system (Peltier et al., 2016). On
136 June 13, 17 and 20, three shallow (hypocentres located above sea level) intense seismic crises
137 occurred below the summit Dolomieu caldera (Fig. 1), with hundreds of events located in a
138 narrow depth range between 1100 and 2100 metres below the volcano summit. These seismic
139 crises consisted of swarms of low magnitude (M: 1-2) volcano tectonic events which
140 increased in number from the first to the third crisis. On June 20, seismicity increased
141 progressively and a final seismic crisis started at 20h20 GMT, only 75 minutes before the
142 eruption. This last seismic crisis was coupled with acceleration in the deformation of the
143 summit area, which began only 60 minutes before the eruption. Interestingly, only slight
144 inflation of the central cone (< 2 cm of dilatation) was detected 11 days before the 2014
145 eruption with a maximum of 1 cm and 1.6 cm enlargement at the summit and the base of the
146 cone, respectively (Peltier et al., 2016 and Fig. 1d). A moderate increase in CO_2 and H_2S
147 emissions from summit intracaldera fumaroles was detected starting on June 2, but only very
148 minor SO_2 emissions occurred before the eruption (mostly on June 7 and 15, unpublished
149 data). Therefore, the acceleration in both geophysical and geochemical parameters was mostly
150 related to the late phase of dyke propagation towards the surface just before the eruption.
151 Following the end of the June 20-21 eruption, a long-term continuous inflation of the edifice
152 began, at a moderate rate, and mostly at the base of the volcano. More than one year after this
153 first eruption, the long-term deformation trends showed that the 2014 eruption marked a kink
154 between the deflation trend which followed the caldera-forming 2007 eruption (Staudacher et
155 al., 2009) and the currently ongoing continuous inflation trend (Fig. 1d, and Peltier et al.,
156 2016; Coppola et al., 2017).

157 **2.2 Chronology of the events**

158 We reconstructed the chronology of the events by combining a distribution map of the
159 fissures, pyroclastic deposits and lava flows (Fig. 1) with a review of available images and
160 videos extracted from the observatory data base, the local newspapers, and web sites (Fig. 2).
161 The 2014 eruption occurred at the summit and on the SE slopes of the Dolomieu Caldera
162 (Figs. 1a, 1b and 1c) and evolved quickly and continuously over 20 hours. The full set of
163 fractures opened during a short period of time (minutes) and emitted short (<1.7 km long)

5

164   lava flows (Fig. 1 and Figs. 2c and 2d). Feeding vents were scattered along a 0.6 km long

165   fissure set (Fig. 1a) and produced very weak (low) Hawaiian to Strombolian activity (Fig. 2).

166   Fissures opened from west to east, initially sub-parallel to the southern border of

167   Dolomieu caldera and then propagated at lower altitude (Fig. 1). The summit part of the

168   fractures (ca. 2500 m asl, Western Fracture, WF in Fig. 1) emitted only small volumes of lava

169   and pyroclasts. This part of the fracture set was active only during the first few hours of the

170   eruption, at night. The eastern part of the fractures (Upper Fracture, UF in Fig. 1) descended

171   to lower altitude (between 2400 and 2300 m asl, Middle Fracture, Fig. 1) along the SE flank

172   of the summit cone and emitted most of the erupted volume. As often observed in PdF

173   eruptions, the activity progressively focused on a narrow portion of the fractures at low

174   altitude and finally on a single vent located at the lower tip of the fracture system (Main Vent,

175   at 2336 m asl, MV in Figs. 1, 2). The first in situ observations in the morning of June 21 (ca.

176   04h00 GMT) showed that weak Strombolian activity (Figs. 2a and 2b) was focused on a

177   narrow segment of the lower fractures and that a'a lavas had already attained the elevation of

178   1983 m asl (0.2 km before maximum runout, Fig. 2c). A small, weak gas plume was also

179   blowing northwards. A single sample of partially molten lava was collected from the still

180   active lava front and partially water quenched (REU140621-1, Table S1, Fig. 2d). During

181   most of June 21, the activity consisted of lava effusion in three parallel lava streams (Fig. 2c)

182   merging in a single lava flow (Fig. 2e) and mild-weak "Strombolian" explosions at several

183   closely spaced spots along the lower part of the feeding fracture. At 13.00 (GMT), only weak

184   explosions were observed within a single small spatter cone (Figs. 2f and 2g). Most of the

185   lava field was formed of open channel a'a lavas. The total volume of lava was estimated by

186   MIROVA service (https://www.sites.google.com/site/mirovaweb/home), with the use of the

187   MODIS images and the analyses of the flux from the spectral properties, to be within 0.34 +/-

188   0.12 x 10^6 m^3, (Coppola et al., 2017). Satellite derived volume estimates are consistent with

189   independent photogrammetric estimates (0.4 ± 0.2 x 10^6 m^3; Peltier et al., 2016) and rank the

190   2014 eruption at the lower end of the volume range typically emitted by PdF (Roult et al.,

191   2012).

192   **3. Methodology**

193   **3.1 Sampling strategy**

194   Apart from the sample from the front of the still active lava flow (Fig. 2d), all other samples

195   were collected in two phases: 3 days (pyroclasts on June 24, Fig. 3a and Table S1) and 11

days after the eruption (lavas on July 2, Table S1), and three months later (pyroclasts from the MV, Fig. 1, on November 18 and Table S1). June 24 samples were collected both from the main fractures (WF and UF, Fig. 1a), the MV and the active lava flow (Fig. 1 and Table S1). Twenty five scoriaceous bombs and lapilli (REU140624-9a-1 to REU140624-9a and REU140624-9b-6 to REU140624-9b-25, in Table S3) were collected from the discontinuous deposit (Fig. 3d) emplaced at the WF site (Fig. 1a), active only at the beginning of the eruptive event. Because of the short duration of the activity at the WF, the scoria fragments on the ground were scarce (Fig. 3d). The strategy was to collect a sample that was formed by the largest available number of clasts that was representative of this discrete deposit (REU140624-9 in Table S1). From the UF (Fig. 1a) only one big scoria was collected (REU140624-13, Table S1) that broke in five parts, allowing us to measure its vesiculated core and the dense quenched external part (REU140624-13-a to REU140624-13-e, in Table S3). In contrast, the sustained and slightly more energetic activity at the lower tip of the fractures, at the MV site, built a small spatter cone (Fig. 2) and accumulated a continuous, small volume deposit (Fig. 3a) of inversely graded scoria fallout (Figs. 3b and 3c). This deposit is 10 cm thick at 2 m from the vent and covers an area of about ~1000 m^2. For this fall deposit we collected two bulk samples, one from the base (within the lower 5 cm, REU141118-6 in Table S1) and the other from the top (within the upper 5 cm, REU140624-3, in Table S1), for the grain size (Fig. 3c) and componentry analyses. The sample at the base was collected in November because on June 24 the loose proximal lapilli blanket was still very hot (405 °C; thermocouple measurement) and fumaroles with outlet temperatures in the range 305-60 °C were sampled all along the fractures several weeks after the eruption (Fig. 1b and Table S1). These latter geochemical data are not presented in this paper. We selected 103 fragments from the coarse grained bulk deposit within the upper 5 cm of the scoria fall out deposit (Fig. 3b) at MV (REU140624-3-1 to REU140624-3-103, in Table S3) for density, connectivity, permeability, petrological and geochemical analysis. In addition, in November 2014, more than 200 clasts (comprising the REU141118-1 to REU141118-5 samples, Table S1) of similar size were collected, both close to the MV and in the 'distal' area (30 metres away from the MV site) to complete the particle bulk texture analyses and the chemical analyses.

3.2 Grain size and componentry

We performed grain size analyses on the two bulk samples collected from the MV, following the procedure of Jordan et al. (2015) (Table S2). The samples were dried in the oven at 90°C

229 and sieved at ½ phi intervals in the range of -5 φ to 4 φ (Fig. 3c); the data are also shown in

230 full phi for comparison with the deposits of the 2010 PdF fountaining episode (Hibert et al.,

231 2015; Fig. 3f). Sieving was carried out by hand and for not longer than three minutes to avoid

232 breaking and abrasion of the very vesicular and fragile clasts. For the scattered scoria sampled

233 from the WF (Figs. 1, 3d and 3e), we followed the grain size strategy proposed in Gurioli et

234 al. (2013). Within this procedure we sampled each fragment and we recorded the weight and

235 the three main axes (a being the largest, b, and c). To allow comparison with the sieving grain

236 size analyses (Inman, 1952), we used the intermediate b axis dimension to obtain $\varphi = -\log_2 b$.

237 Following the nomenclature of White and Houghton (2006) the componentry analysis

238 is the subdivision of the sample into three broad components: i) juvenile, ii) non-juvenile

239 particles, and iii) composite clasts. The juvenile components are vesicular or dense fragments,

240 as well as crystals, that represent the primary magma involved in the eruption; non-juvenile

241 material includes accessory and accidental fragments, as well as crystals that predate the

242 eruption from which they are deposited. Finally, the composite clasts are mechanical mixtures

243 of juvenile and non-juvenile (and/or recycled juvenile) clasts. In these mild basaltic

244 explosions, the non-juvenile component is very scarce, so we focused on the juvenile

245 component that is characterized by three groups of scoria: (i) spiny-opaque, (ii) spiny-glassy,

246 and (iii) fluidal, along with golden pumice (Fig. 4). The componentry quantification was

247 performed for each grain size fraction between -5 φ to 0.5 φ (Figs. 5a and 5b), where a

248 binocular microscope was used for the identification of grains smaller than -1 phi (Table S2).

249 In the following, we will use the crystal nomenclature of Welch et al. (2009), with the

250 strictly descriptive terms of macrocrysts (> 3 mm in diameter) mesocrysts (from 0.3 to 3 mm

251 in diameter), and microcrysts (<0·3 mm in diameter). Regarding the June 2014 products,

252 these ranges of size may however change in comparison to the December 2005 products

253 studied by Welsch et al. (2009).

3.3 Particle bulk texture (density, porosity, connectivity, permeability) and microtexture

255 For each sample site (WF, UF and MV, Fig. 1a), we selected all the available particles within

256 the 8-32 mm fraction for density/porosity, connectivity and permeability measurements (Table

257 S3). This is the smallest granulometric fraction assumed to be still representative of the larger

258 size class in terms of density (Houghton and Wilson, 1989; Gurioli et al., 2015), and has been

259 used in previous textural studies (e.g., Shea et al., 2010). In addition, this size range is ideal

260 for vesicle connectivity measurements (e.g. Formenti and Druitt, 2003; Giachetti et al., 2010;

261 Shea et al., 2012; Colombier et al., 2017a, b). Density of juvenile particles was measured by

8

262 the water-immersion technique of Houghton and Wilson (1989), which is based on
263 Archimedes principle. A mean value for the vesicle-free rock density was determined by
264 powdering clasts of varying bulk densities, measuring the volumes of known masses using an
265 Accupyc 1340 Helium Pycnometer, then averaging. The same pycnometer was also used to
266 measure vesicle interconnectivity for each clast using the method of Formenti and Druitt
267 (2003) and Colombier et al. (2017a). Permeability measurements were performed on five
268 clasts: two golden pumices, one fluidal, one spiny glassy and one opaque scoria, all collected
269 from the MV (Table S3). Following Colombier et al. (2017a), the clasts were cut into
270 rectangular prisms to enable precise calculation of the cross-sectional area, which is required
271 to calculate permeability. These prisms were then embedded in a viscous resin, which was left
272 to harden for 24 h. The sample surface had been previously coated with a more viscous resin
273 and then wrapped with parafilm to avoid intrusion of the less viscous resin inside the pores.
274 The coated samples were placed with a sample holder connected to a permeameter built at
275 Laboratoire Magmas et Volcans (LMV, France) following Takeuchi et al. (2008). The
276 measurements were performed at atmospheric pressure (i.e. without confining pressure) and
277 the samples were measured at a range of gas flow rates and upstream air pressures to create a
278 curve that could be fitted using a modified version of Darcy's Law, the Forchheimer equation,
279 to solve for viscous (k_1) and inertial permeabilities (k_2) (Rust and Cashman, 2004, Lindoo et
280 al. 2016 and Colombier et al. 2017).

281   Vesicle size distribution was performed following the method of Shea et al. (2010) and
282 Leduc et al. (2015), while the total crystallinity, the percentages for both crystal phases
283 (plagioclase and clinopyroxene) and size-populations (meso and microcrysts) were calculated
284 using the raw data from FOAMS program (Shea et al 2010) and the CSDcorrections program
285 of Higgins (2000) and the CSDslice data base (Morgan and Jerram 2006) to have the
286 percentage of crystals in 3D with the corrected assumption for shape. We performed these
287 analyses on eight clasts picked up from each component-density distribution (stars in Figs. 6a
288 and 6b). The choice of the clasts was made mostly on the typologies, rather than on each
289 density distribution, in order to avoid the analysis of clasts with transitional characteristics.
290 For example, two golden pumice fragments were selected from the largest clasts that were the
291 less dense and didn't break, even if the values in vesicularity were similar. A larger number of
292 fluidal fragments were chosen (even if the density distribution was unimodal) because this
293 typology of clasts was the most abundant and was emitted all along the active fracture, so we
294 did our best in order to study products representative of the WF, the UF and the MV activities.
295 Only one spiny glassy and one spiny opaque were selected, because they were emitted only at

296 the MF. A full description of the textural measurements all performed at LMV, as well as the
297 raw data of these measurements are available at DynVolc Database (2017).

298 **3.4 Bulk geochemistry**

299 For the determination of the bulk chemistry (Table S4 and Fig. 7) of the different pyroclasts
300 we selected the largest pyroclasts of golden pumice and the largest fluidal, spiny glassy and
301 spiny opaque scoriae (Table S4). We also analyzed two fragments of lava, from the beginning
302 and the end of the eruption (Table S4). Samples were crushed into coarse chips using a steel
303 jaw crusher and powdered with an agate mortar. Major and trace element compositions were
304 analyzed using powder (whole rock composition). In addition, for a sub-set of pyroclasts,
305 glass chips (2-5 mm in size) were hand-picked under a binocular microscope and analyzed
306 separately for trace elements. For major element analysis, powdered samples were mixed with
307 $LiBO_2$, placed in a graphite crucible and melted in an induction oven at 1050 °C for 4.5
308 minutes, resulting in a homogeneous glass bead. The glass was then dissolved in a solution of
309 deionized water and nitric acid (HNO_3), and finally diluted by a factor of 2000. The final
310 solutions were analyzed by ICP-AES. Trace element concentrations were analysed following
311 a method modified from Vlastélic et al. (2013). About 100 mg of sample (powder and chip)
312 were dissolved in 2 ml of 28M HF and 1 ml of 14M HNO_3 in teflon beaker for 36 hours at
313 70°C. Solutions were evaporated to dryness at 70°C. The fluoride residues were reduced by
314 repeatedly adding and evaporating a few drops of concentrated HNO_3, before being fully
315 dissolved in ca. 20 ml of 7M HNO_3. These solutions were diluted by a factor of 15 with
316 0.05M HF (to reach rock dilution factor of ca. 4000) and trace element abundances were
317 determined by quadrupole ICPMS (Agilent 7500). The analyses were performed in plasma
318 robust mode (1550 W). The reaction cell (He mode) was used to reduce interference on
319 masses ranging from 45 (Sc) to 75 (As). The signal was calibrated externally (every 4
320 samples) with a reference basaltic standard (USGS BHVO-2) dissolved as for the samples and
321 using the GeoRem recommended values (http://georem.mpch-mainz.gwdg.de/). For elements
322 that are not well characterized in literature (As, Bi, Tl), or which show evident heterogeneity
323 (e.g. Pb) in BHVO-2 powder, the signal was calibrated using the certified concentrations of a
324 synthetic standard, which was also repeatedly measured. The external reproducibility (2σ
325 error) of the method is 6% or less for lithophile elements and 15% or less for chalcophile
326 elements.

327 **3.5 Glass and crystal chemistry**

328 Spot analyses of matrix glass and crystal composition (Table S5) were carried out using a

329 Cameca SX100 electron microprobe (LMV), with a 15 kV acceleration voltage of 4 nA beam

330 current and a beam of 5 μm diameter for glass analyses. However, for the spiny opaque

331 scoria, characterized by abundant crystals with rapid growth textures, a voltage of 8 nA beam

332 current and a beam of 10 μm diameter were used. For this latter sample, 10 analyses per

333 sample were performed due to the heterogeneity within the highly crystallised glass (Fig. 8a),

334 while for the other samples 6 analyses per sample were enough to characterize the clean

335 homogeneous glass. For crystal analysis, a focused beam was used. For the characterization of

336 the meso- and micro-crysts, due to their small size, only two to three measurements were

337 performed, one at the edge, one in the middle and one at the core of the crystals, to check for

338 possible zonation.

339 **3.6 Melt inclusions**

340 Melt inclusions (MIs; Table S6, Figs. 8b and 9) were characterized in the olivine mesocrysts

341 from the three groups of scoriae (fluidal, spiny glassy and spiny opaque), but not in the

342 pumice group, because crystals were too rare and small to be studied for MIs.

343   Olivine crystals were handpicked under a binocular microscope from the 100– 250 and

344 250– 600 μm grain size fractions of crushed tephra. Crystals with MIs were washed with

345 acetone, embedded in epoxy and polished individually to generate adequate exposure of the

346 MIs for *in situ* electron probe microanalysis. The MIs are spherical to oblate in shape and

347 range in size from 10 to 200 μm. Some of the MIs contain shrinkage bubbles but all of those

348 studied are totally deprived of daughter minerals. Major elements were measured on a

349 Cameca SX-100 microprobe at LMV (Table S6). For major elements, the larger MIs were

350 analyzed with a spot diameter of 10-20 μm and sample current of 8 nA, whereas the smaller

351 MIs were analyzed with a beam of 5 μm and a sample current of 4 nA. The results are given

352 in Table S6, and analytical details and uncertainties are listed in Óladóttir et al. (2011) and

353 Moune et al. (2012).

354 **4 Results**

355 **4.1 Deposit texture (grain size, componentry, morphology) and petrological description**

356 **of the samples**

357 The pyroclastic deposits at the WF and UF sites (Fig. 1a) are formed by scattered

358 homogeneous smooth fluidal (Figs. 3d) bombs and lapilli scoria. The average dimension of

11

359 the fragments is around 4 cm (maximum axis) with bombs up to 10 cm and scoria lapilli up to

360 2 cm in size (Fig. 3e).

361   At the MV, the reversely graded deposit (Fig. 3b) is made up of lapilli and bombs, with

362 only minor coarse ash (Fig. 3c). The lower 5 cm at the base are very well-sorted and show a

363 perfect Gaussian distribution with a mode at 4 mm (Fig. 3c). In contrast, the grain size

364 distribution of the upper 5 cm is asymmetrical with a main mode coarser than 22 cm and a

365 second mode at 8 mm (Fig. 3c). This upper deposit is negatively skewed due to the abundance

366 of coarse clasts. The dataset shows a similarity between the grain size distributions of the

367 basal tephra ejected from the 2014 MV and the ones for the lava fountaining of the 2010

368 summit event (Fig. 3f and Hibert et al., 2015). On the contrary, the top of the 2014 fall differs

369 from fountain deposits, being coarser and polymodal, and it is ascribed to dominantly

370 Strombolian activity (Fig. 3f).

371   In terms of componentry of the deposits, four types of clasts were distinguished (Fig.

372 4): (i) golden pumice, (ii) smooth or rough fluidal scoriae, (iii) spiny glassy scoria, (iv) spiny

373 opaque scoria. The pumices are vesicular, low-density fragments, characterized by a golden to

374 light brown color, sometimes with a shiny outer surface (Fig. 4a). They are usually rounded in

375 shape. Golden clasts studied for textures contain a few microcrysts of plagioclase (up to 0.1

376 mm in diameter), clinopyroxene up to 0.05-0.06 mm in diameter, and small olivine up to 0.03

377 mm in diameter (Fig. 4), together with large areas of clean, light brown glass. The fluidal

378 scoria fragments have dark, smooth or rough shiny surfaces (Fig. 4b). They can be more or

379 less elongated in shape and have spindle as well as flattened shapes. The fluidal fragments are

380 characterized by rare mesocrysts of plagioclase and clinopyroxene and microcrysts of

381 plagioclase, clinopyroxene and olivine (Fig. 4b). The spiny glassy fragments are dark, spiny

382 scoria that range in shape from subrounded to angular (Fig. 4c). These fragments contain

383 abundant glassy areas, while the spiny opaque fragments lack a glassy, iridescent surface.

384 Both groups of spiny clasts are characterized by the presence of dark and light brown glass.

385 The spiny opaque fragments are the densest fragments and have the largest amount of

386 crystals. They contain, as the most abundant phase, relatively large meso- and micro-crysts of

387 plagioclase, up to 3 mm long, together with meso- and micro-crysts of clinopyroxene and

388 olivine (Figs. 4c and 4d). In the dark portions of their matrix, tiny fibrous microcrysts of

389 olivine + clinopyroxene + plagioclase + Fe-Ti oxides occur. The spiny glassy fragments have

390 the same crystal populations as the spiny opaque ones, but their plagioclases are much smaller

391 and attain a maximum length of only 0.3 mm. Clusters of plagioclase and clinopyroxene are

392 present in both the spiny opaque and the spiny glassy fragments, as well as rare macrocrysts

12

393   of olivine. The olivine macrocrysts exhibit the typical compositional (Fo 84.2) and

394   petrographic features of olivine phenocrysts described in previous studies (Clocchiatti et al.,

395   1979; Albarede and Tamagnan, 1988; Bureau et al., 1998a and b; Famin et al., 2009; Welsch

396   et al., 2013). They are automorphic, fractured with oxides (mostly chromite) and melt

397   inclusions (Fig. 4c). Fluidal and pumice fragments studied for textures contain rare

398   macrocrysts and mesocrysts of olivine, and the crystals are essentially microcrysts. The

399   pumice and some fluidal fragments have lower contents of microcrysts than some fluidal and

400   spiny fragments, with the latter having the highest microcryst content (Table S4). For

401   comparison two fragments of lava have been analyzed as well (Table S3). The lava fragments

402   are poorly vesiculated and completely crystalline (Fig. 4e). The lava contains the same

403   paragenesis of crystals described in the spiny opaque fragments, with the main difference that

404   its matrix is completely crystallized and constituted mostly by well-formed plagioclase up to

405   800 microns and clinopyroxene up to 500 microns. Scarce, smaller olivines, are also present

406   Ubiquitous tiny rounded Fe-Ti oxides provide evidence of post emplacement crystallization.

407   The componentry results are reported in Figure 5 for the MV deposits; being the

408   deposits from the WF and UF characterized exclusively by fluidal clasts (Fig. 3). At the base

409   of the MV deposit, the coarse fraction of the deposit is rich in golden and fluidal components

410   that represent more than 60-70 vol. % (Figs. 5a and 5b). The proportion of the two groups is

411   similar. In contrast, in the upper, coarse grained fall deposit, the clasts bigger than 8 mm are

412   dominated by the spiny scoria fragments, while the fraction smaller than 8 mm show a

413   dramatic increase in the golden and fluidal fragments, with the fluidal ones always more

414   abundant than the golden ones (Figs. 5a and 5b). Abundant low-density, golden, coarse lapilli

415   pumice and bombs have been found scattered laterally up to 30 metres from the main axis and

416   were not found in the proximal deposit. On the basis of the high amount of pumice in the

417   lower part of the deposit, we correlate the large, low-density clasts with the base of the

418   proximal deposit, and consequently we interpret them as material emitted at the beginning of

419   the June 2014 eruptive event.

420   **4.2 Particle density, porosity, connectivity, permeability and micro-texture**

421   Density analyses performed on 200 coarse lapilli reveal a large variation in density values

422   from 390 kg/m^3 to 1700 kg/m^3 with a median value at 870 kg/m^3 (Table S3). The fragments

423   collected from the MV have a bimodal density distribution, with a main population of low-

424   density fragments having a mode at 800 kg/m^3, and a second and denser population centered

425   at 1400 kg/m^3 (Fig. 6a). The golden and fluidal fragments form the lower-density population

13

426 and the spiny fragments are dominant in the denser population (Fig. 6a). For these samples

427 there is a marked correlation between porosity and morphology, so that the spiny-opaque

428 clasts are the densest (up to 1600 kg m^{-3}, with a vesicularity of 45 vol. %) and the golden

429 pumice are the least dense (minimum density of 390 kg m^{-3} with a vesicularity of up to 86 vol.

430 %; with a Dense Rock Equivalent density of 2880 kg m^{-3}). The fluidal fragments collected at

431 the WF (Fig. 1b), have a density range from 700 to 1400 kg m^{-3} and a mode at 1000 kg m^{-3}

432 (Fig. 6b). The five fragments from the only bomb collected at the UF are characterized by two

433 distinct density values, the low density one (700-800 kg m^{-3}) refers to the core of the sample,

434 while the high density one (1400-1500 kg m^{-3}) represents the quenched external rim of the

435 bomb. Finally, the two fragments of lava show the highest density values at 1800 and 2150 kg

436 m^{-3}. This last value is one of the highest found in the lava collected from 2014 up to 2017 (see

437 Fig. 13 in Harris et al., 2017 and unpublished data).

438 In all these samples, the increase in vesicularity correlates with an increase in the

439 amount of small (0.1 mm), medium (0.5-1 mm) and large (up to 4 mm) vesicles. In the fluidal

440 clasts, these vesicles have a regular rounded or elliptical shape and are scattered throughout

441 the sample. The low-density pumices are often characterized by the presence of a single, large

442 central vesicle (10 – 15 mm) with the little vesicles and a few medium vesicles distributed all

443 around it (Fig. 4). The spiny glass texture is characterized by a lower amount of small vesicles

444 than in the pumice and by the presence of mostly medium sized vesicles, while the spiny

445 opaque has more irregular shape, very large (up to 10 mm) vesicles with a small and a

446 medium sized bubble population. In the spiny glass samples, the glass is more or less brown,

447 with the dark brown portions being the ones with the lowest vesicle content and the highest

448 microcrysts content. The opaque samples have a central, very dark glass portion, with low

449 vesicle content, and a more vesicular glassy portion at the outer edges (Fig. 4). The two

450 fragments of lava are poorly vesiculated (Fig. 6a) and characterized by large, irregular

451 vesicles (up to 5 mm in diameter). Clusters of small vesicles (up to 0.1 mm) are scattered

452 between the large ones.

453 The vesicle size distribution (VSD in Fig. 4) histograms are characterized by a

454 decrease in percentage of vesicles from the golden to the lava as well as an increase in

455 coalescence and or expansion signatures in the spiny fragments, marked by the increasing of

456 the large vesicles population (Figs 4c and 4d). This trend is also marked by the decrease in

457 number of vesicle per unit of volume (N_v, Fig. 4) from the golden to the lava. Finally, the

458 trend is also mirrored by the total percentage of crystals (calculated in 3D, Fig. 4 and reported

459 for each sample in Table S3) that increases with the increase of density of the clasts, from a

14

460 minimum of 8 vol. % for the golden up to 55 vol. % for the spiny opaque scoria, and 100 vol.

461 % for the lava (Fig. 4). Mesocrystals, formed mostly by the same proportion of plagioclase

462 and clinopyroxenes, are absent or very scarce in the golden and fluidal fragments, while they

463 reach their maximum values, up 21 vol. % in the spiny opaque fragment. The population of

464 microcrystals is mostly constituted by plagioclases that range from a minimum of 6 vol. % in

465 the golden, up to 23-25 vol. % in the spiny fragments and to 64 vol. % in the lava.

466   The connectivity data (Fig. 6c) also indicate that the fluidal and golden clasts have a

467 larger amount of isolated vesicles (up to 40 vol. %) with respect to the spiny products. The

468 fluidal clasts from the WF are the most homogeneous with an average percentage of isolated

469 vesicles around 30 vol. %. In contrast, both the pumice and the fluidal fragments from the

470 MV, characterized by higher values of porosity (> 75%), have a wide range in percentage of

471 isolated vesicles (between 20 and a few vol. %). The fragments of the bomb collected at the

472 UF are consistent with a vesiculated core characterized by scarce isolated vesicles and the

473 quenched rind that has 30 vol. % of isolated vesicles. Finally the spiny fragments have the

474 lowest content of isolated vesicles (0-5 vol. %). Despite the presence of these isolated

475 vesicles, all the samples shear high values of permeability, with the Darcian (viscous, K_1)

476 permeability values ranging from 10^{-11} to 10^{-10} m^2 (Fig. 6d and Table S3). The graph of

477 vesicularity versus K_1 shows a slightly increase in permeability with vesicularity, being the

478 golden pumice the most permeable among the samples and the spiny glassy fragment the least

479 permeable. The three samples collected from the February 2015 eruption fit this trend.

480 However, the densest spiny opaque scoria of the 2014 eruption shares the high permeability

481 value of the golden pumice.

482 **4.3 Chemistry of the products**

483 Major and trace element concentrations of whole-rock and hand-picked glass samples are

484 reported in Table S4. Whole rock major element composition is very uniform (e.g.,

485 6.5<MgO<6.7 wt%) and well within the range of Steady State Basalts (SSB), the most

486 common type of basalts erupted at PdF (Albarède et al., 1997). However, compatible trace

487 elements, such as Ni and Cr, are at the lower end of the concentration range for SSB

488 (<100ppm) indicating that the June 2014 eruption sampled relatively evolved melts. Ni and Cr

489 generally show higher concentrations in 2014 bulk rocks (79<Ni<92ppm and 71<Cr <87ppm)

490 compared to the 2014 glass chips (66<Ni<73ppm and 54<Cr <59ppm for all but two chips).

491 In the Cr vs Ni plot (Fig. 7a), whole rocks plot to the right of the main clinopyroxene +/-

492 plagioclase–controlled melt differentiation trend. This shift reflects the addition of Ni-rich

15

493   olivine (Albarède and Tamagnan, 1988). We estimate that the Ni excess results from the

494   occurrence of a low amount (0.7 to 1.3 wt%) of cumulative olivine in whole rocks, consistent

495   with thin section observations. The composition of olivine macrocrysts (ca. Fo84) is too

496   magnesian to be in equilibrium with the low-MgO evolved composition of the 2014 magma.

497   Using our estimate for the amount of cumulative olivine, we recalculate the olivine–corrected

498   MgO content of the 2014 magma at 6.2 wt%. The June 2014 melt is thus only moderately

499   depleted in compatible elements compared to the previous eruption of December 2010

500   (MgO~6.6 wt%, Ni~80 ppm, Cr~120 ppm). Conversely, the June 2014 melt is significantly

501   depleted in compatible elements compared to the earlier November 2009 eruption, which

502   sampled relatively primitive magmas (average MgO~7.7 wt%, Ni~135 ppm, Cr~350 ppm)

503   (Fig. 7a). The 2014 evolved composition plots at the low-Ni-Cr end of PdF historical

504   differentiation trend (Albarède and Tamagnan, 1988), near the composition of lavas erupted

505   on 9 March 1998 after 5.5 years of quiescence (1992-1998). Note that olivine accumulation at

506   PdF generally occurs in melt having ca.100 ppm Ni (Albarède and Tamagnan, 1988). Olivine

507   accumulation in evolved melts (Ni < 70 ppm) seems to be a distinctive feature of many small

508   post-2007 eruptions (e.g. this event and the three 2008 eruptions, see Di Muro et al., 2015).

509   A closer inspection of Ni-Cr variability in June 2014 whole rock samples (Fig. 7b)

510   reveals that scoria from the WF (140624-9b-6, Table S4) and early erupted lavas (1406-21-1,

511   Table S4) have the lowest amount of olivine (<0.9%) whereas scoria from the UF (140624-

512   13a) and late erupted lavas (140324-12) have a slightly higher amount of olivine (>1.2%).

513   This is consistent with the general trends observed at PdF of olivine increase from the start to

514   end of an eruption (Peltier et al., 2009).

515   The so called "olivine control trend" in Ni-Cr space cannot be explained either by

516   addition of pure olivine, which contains less than 500 ppm Cr (Welsch et al., 2009; Salaün et

517   al., 2010; Di Muro et al., 2015), or by the addition of olivine plus pyroxene (which would

518   require ca. 50% pyroxene with 970 ppm Ni and 4800 ppm Cr, see Fig. 7 caption). Instead,

519   addition of olivine hosting ca. 1% Cr-spinel (with 25 wt.% Cr) accounts for data and

520   observations, and is consistent with crystallization of olivine and Cr-spinel in cotectic

521   proportions (Roeder et al., 2006). The fact that some samples (golden pumice) plot off the

522   main, well-defined array, can be explained either by addition of more or less evolved olivine

523   crystals (within the range of Fo 80-85 measured in June 2014 samples) and/or slight

524   variations ($\pm$ 0.02%) in the proportion of Cr-spinels (Fig. 7b).

525   The glass chemistry of the four clast types allows us to correlate porosity and oxide

526   contents and shows an increase in MgO from the spiny opaque to fluidal and golden

16

527 fragments (Fig. 8a). Consistent with petrological and textural observations, the spiny opaque

528 is the most heterogeneous type of clast in terms of glass composition (Fig. 8). The glassy

529 portion at the edge of the clast is similar to the spiny glass, while the interior, characterized by

530 dark areas rich in tiny fibrous microcrysts, shows scattered glass compositions with very low

531 MgO content as well as a decrease in CaO (Fig. 8). We attribute the significant variation in

532 glass composition within the different components to variable degrees of micro-crystallisation

533 as the bulk chemistry of all clasts is very similar and globally homogeneous.

4.4 Melt inclusions

535 MI analyses must be corrected for post-entrapment host crystallisation at the MI - crystal

536 interface. We used a Kd = $(FeO/MgO)_{ol}$ / $(FeO/MgO)_{melt}$ = 0.306 (Fisk et al., 1988; Brugier,

537 2016) and an average $Fe^{3+}/\Sigma Fe_{total}$ ratio of 0.11 (Bureau et al., 1998a; Di Muro et al., 2016 and

538 references therein) defined for PdF magmas. For the June 2014 melt inclusions, the post

539 entrapment crystallization (PEC) ranges from 2.9 to 10.5 wt%. Raw and corrected major and

540 volatile element concentrations of MIs are reported in Table S6.

541 Host olivines span a large compositional range from Fo_{80} to Fo_{86}. Despite the evolved

542 bulk composition of the magma, most olivines are quite magnesian (Fo_{83-85}) and are not in

543 equilibrium with the evolved host magma. On the contrary, Mg-poor olivines (Fo_{80-81}) can be

544 considered as being in equilibrium with the bulk rock composition. The corrected

545 compositions of MIs in phenocrysts from the different samples partly overlap with the

546 evolved bulk rocks (MgO_{wr}: 6.1-7.2 wt%) and extend to higher MgO contents of up to 8.8

547 wt% (Table S6). MIs display a narrow range of transitional basaltic compositions (K_2O= 0.5-

548 0.9 wt%) and show no significant difference between the three types of scoriae. The major

549 element composition of melt inclusions correlates with that of the host olivines. Melt

550 inclusions in the high Fo-olivines have the highest MgO, CaO and TiO_2 and lowest K_2O

551 concentrations (Table S6). It is interesting to note that the June 2014 products contain two

552 populations of magnesian ($Fo_{>83}$) olivines hosting melt inclusions with two distinct Ca

553 contents. Most of the magnesian olivines contain MIs with unusually high CaO contents (11.6

554 – 12.9 wt%) and high CaO/Al_2O_3 ratios (0.8-0.9), higher than that of the bulk rocks (0.8) (Fig

555 8). The occurrence of olivines with "high Ca" melt inclusions has been observed in all three

556 different types of scoriae. A few magnesian olivines and all Mg-poor olivines ($Fo_{80.5-83.6}$) host

557 MIs with lower CaO contents (11.4 wt%). This latter composition overlaps with that of the

558 bulk rock (Fig 8). The "high Ca" population of inclusions is also enriched in TiO_2 and Al_2O_3

and depleted in MgO, FeO_T and Na_2O for a given olivine Fo content with respect to the "low Ca" population. Both low- and high-Ca populations of melt inclusions have similar K_2O contents and total alkali content increases from 3 wt% at 12.6 wt% CaO, to 3.5 wt% at 10.8 wt% CaO. However, we remark that high Ca melt inclusions from the June 2014 activity record a significant scattering in K_2O contents, which range from 0.55 to 0.9 wt%. These anomalous compositions potentially track processes of crystal dissolution (e.g. pyroxene dissolution).

MIs in olivines from June 2014 can best be compared with those of other recent small-volume and short-lived eruptions which emitted basalts with low phenocryst contents, like those in March 2007 (0.6×10^6 m^3) and November 2009 (0.1×10^6 m^3) (Roult et al., 2012). March 2007 aphyric basalt has a bulk homogeneous composition with intermediate MgO content (MgO_{wr}: 7.33 wt%; K_2O: 0.67 wt%). Their olivines (Fo 81) are in equilibrium with the bulk rock and their composition is unimodal (Di Muro et al., 2014). November 2009 products are the most magnesian lavas emitted in the 2008-2014 period, slightly zoned (MgO_{wr}: 7.6-8.3 wt%; K_2O: 0.75 – 0.62 wt%) and contain a few percent of normally zoned olivine macrocrysts with bimodal composition (Fo81 and Fo83.5, see Di Muro et al., 2016). June 2014 bulk rocks (MgO_{wr}: 6.7 wt%; K_2O: 0.75 wt%) and melt inclusions in Fo_{80-81} olivines are quite evolved. Their composition is close to that of products emitted by summit intracaldera eruptions in 2008, ca. 1.5 years after the large 2007 caldera forming eruption (Di Muro et al., 2015) (Fig. 8). As already reported for 2008 products, many olivine macrocrysts of 2014 are clearly too magnesian to be in equilibrium with the relatively evolved host melts. Overall, MgO content in 2007-2014 melt inclusions tends to decrease with decreasing Fo content of the host olivines. MIs in olivines also exhibit a trend of linear decrease in MgO and increase in FeO from April 2007 to 2009-2014 products (Fig. 9). Melt inclusions in March 2007, November 2009 and June 2014 follow the same trend of FeO enrichment (Fig. 9). In the large-volume and olivine-rich April 2007 products, MIs in magnesian olivines with $Fo_{>82}$ have distinctly higher MgO, FeO and lower SiO_2 and Al_2O_3 than MIs in 2009-2014 products. The distinctive FeO enrichment of many of the MIs from the April 2007 oceanite has been interpreted by Di Muro et al. (2014) as a result of post-entrapment modification related to new magma inputs into long lasting magma storage.

Two populations of low- and high-Ca melt inclusions are also found in the November 2009 olivines. Low-Ca melt inclusions from the November 2009 and June 2014 eruptions indicate a single trend of chemical evolution (Fig. 8), consistent with bulk rock compositions. June 2014 products have lower MgO and CaO contents than those from November 2009.

18

593 Significant scattering in K_2O content (0.6-0.9 wt%) is found in low-Ca inclusions from 2009,

594 as observed in high-Ca inclusions from the 2014 eruption, but they share similar K_2O

595 contents. In 2009 and 2014 products, K_2O content of melt inclusions is partly anti-correlated

596 with the olivine Fo content. This observation has been attributed to moderate heterogeneity of

597 primary melts feeding the plumbing system of PdF. Rapid temporal changes of K_2O content in

598 PdF basalts have been reported (Boivin and Bachelery, 2009).

4.5 Mineral composition and glass – plagioclase equilibrium

600 All 2014 scoriae (spiny, fluidal, golden) contain the same paragenesis of olivine,

601 clinopyroxene and plagioclase. The composition of minerals found in golden, fluidal and

602 spiny scoriae is indistinguishable.

603 In olivines, average MgO content decreases from macrocrysts ($Fo_{84.1}$) to mesocrysts

604 ($Fo_{79.6}$) to microcrysts. Olivine microcrysts (Table S5) are normally zoned. Their composition

605 ranges from $Fo_{78.0-75.3}$ in the cores to $Fo_{74.3-70..5}$ in the rims. Overall, olivines in 2014 products

606 span the full range of typical Fo contents of recent PdF magmas (Boivin and Bachèlery, 2009;

607 Di Muro et al., 2014; 2015). Clinopyroxene composition (augites) ranges from $En_{53}Fs_{15}Wo_{32}$

608 to $En_{41}Fs_{14}Wo_{45}$. Their average composition ($En_{45}Fs_{14}Wo_{41}$) is consistent with that found in

609 other recent evolved melts like those emitted by the 2008 eruptions (Di Muro et al., 2015) and

610 more generally in recent PdF products (Boivin and Bachèlery, 2009). Clinopyroxenes are

611 unzoned, the composition of cores and rims is very similar and close to that found in

612 microcrysts and mesocrysts. Plagioclase composition ranges from $An_{79.5}Ab_{19.9}Or_{0.6}$ to

613 $An_{63.1}Ab_{35.7}Or_{1.2}$ with a bimodal distribution ($An_{76.5-79.5}$ and $An_{63.1-72.9}$, Fig. 10a). Similar

614 bimodal distributions were observed in many other products at PdF (Di Muro et al., 2015).

615 Mesocrysts ($An_{75.5}Ab_{23.8}Or_{0.7}$ on average) are more calcic with respect to microcrysts

616 ($An_{65.7}Ab_{33.1}Or_{1.2}$ on average). Normal zoning is found from plagioclase cores to rims (Fig.

617 10a). The composition and zonation of 2014 plagioclases clearly contrast with the complex

618 and often reverse zoning patterns and intermediate composition of the 2008 PdF products that

619 were attributed to pre-eruptive magma heating (Di Muro et al., 2015).

620 Plagioclase-melt equilibrium and melt composition in pyroclastic rocks and water-

621 quenched lavas were used to estimate both temperature and water content dissolved within the

622 melt (Fig. 10b and Table S5). Temperature estimates are based on the (dry) equation of Helz

623 and Thornber (1987) recalibrated by Putirka (2008). Dissolved water content was calculated

624 from the plagioclase hygrometer of Lange et al. (2009) at 50 MPa. This pressure corresponds

625 to the average CO_2-H_2O saturation pressure (recalculated with Papale et al., 2006) typically

19

626 recorded in melt inclusions from central products at PdF (e.g. 1931 eruption in Di Muro et al.,
627 (2016) and references therein). This pressure roughly corresponds to the sea level depth,
628 which is inferred to be the location of the potential main shallow magmatic reservoir (Peltier
629 et al., 2009; Lengliné et al., 2016; Coppola et al., 2017). The application of the plagioclase
630 hygrometer of Lange et al. (2009) makes it possible to estimate the dissolved water content in
631 the melt with a nominal uncertainty of 0.15 wt% and is only slightly dependent on pressure.
632 Plagioclase compositions not in equilibrium with the melt (glass or bulk rock) are those of
633 mesocryst cores with the highest ($An_{>76.5}$) anorthite content (Fig. 10a and Table S5). Such
634 compositions are more in equilibrium with CaO-richer magnesian melts than those measured
635 in matrix glasses and bulk rocks of 2014 eruption and likely formed during early stages of
636 shallow magma differentiation (Fig. 10a).

637 In order to determine pre-eruptive conditions, calculations were performed only on
638 paired plagioclase rims and matrix glasses in equilibrium, using the plagioclase-melt
639 equilibrium constant of Putirka (2008) calibrated for melts whose temperature exceeds
640 1050°C ($Kd_{An-Ab} = 0.27 \pm 0.05$). Our review of published and unpublished data shows that melt
641 temperature progressively decreases from April 2007 (1188+/-16 °C) to January-October
642 2010 (1147+/-9°C) and positively correlates with K_2O content in melts which increases from
643 0.70 to 0.96 wt% (Fig. 10b). The melts from the June 2014 eruption record the lowest
644 temperatures in post-2007 eruptions (1131±15 °C) together with the highest K_2O-enrichment
645 (K_2O: 0.90±0.12 wt%). The lowest temperatures are recorded by spiny scoriae, while the
646 temperature of golden scoriae overlaps with that of 2010 products emitted before the 2010-
647 2014 phase of quiescence. In spite of the large variability in melt composition and
648 temperature, average pre-eruptive water content dissolved in the melts (0.5 +/- 0.2 wt%) is
649 quite homogeneous for the whole 2008-2014 period. In 2014, the lowest estimated dissolved
650 water content (down to 0.38 wt%) is for the golden and some fluidal scoriae, while the
651 maximum amount (0.68 wt%) is for the spiny opaque scoriae. However, water content
652 estimated from core-bulk rock equilibrium (0.3±0.1 wt%) is slightly lower than that estimated
653 from rim and microlite-matrix glass equilibrium (0.5±0.2 wt%), but the difference broadly
654 overlaps the nominal uncertainty related to calculations. Dissolved water contents in melts of
655 the pyroclasts are thus intermediate between those measured in 2007 melt inclusions (H_2O:
656 0.8 +/- 0.15 wt% and up to 1.1 wt%) and those typically found in degassed matrices of lava
657 and Pele's hairs of 2007 (Fig. 10b; 0.2 wt%; see Di Muro et al., 2015; 2016).

658 **5 Discussions**

20

5.1 Eruptive dynamics

The activity fed by the uppermost WF and UF (Fig. 1) was very short-lived, as shown by the presence of only scattered bombs and coarse lapilli (Figs 3d and 3e). The homogeneity of these clasts, their coarse grained nature and the fluidal smooth texture are in agreement with very short-lived fire-fountaining/magma jets. Glassy outer surfaces of clasts have been interpreted as a late-stage product of fusion by hot gases streaming past the ejecta within the jet/fountain (Thordarson et al., 1996; Stovall et al., 2011). However, the occurrence of this process is not supported by the homogeneous glass composition in our fluidal clasts. Therefore, we interpret these features here just as rapid quenching and not re-melting. Vlastélic et al. (2011) documented the mobility of alkalis and other elements on PdF clasts that experienced long exposures to acid gases. In the 2014 eruption pyroclasts, the mobility of elements was prevented by the short duration of the events.

At lower altitude and close to the MV (Fig. 1), the 5 cm layer at the base of the fall deposit is fine-grained (Figs. 3b and 3c), rich in fluidal and golden fragments (Fig. 5), with a perfect Gaussian grain size curve (Fig. 5), and similar to that reported from the weak 2010 fountaining event (Fig. 3f and Hibert et al., 2015). Therefore, we interpret this deposit as being due to weak Hawaiian like fountaining (sustained, but short-lived) activity. We want to remark here that this activity happened during the night and was not observed. The top of the same deposit is coarse grained (Figs 3b and 3c), bimodal, has a lower content in coarse ash (Table S2) and is rich in spiny opaque and spiny glass fragments (Fig. 5). The reverse grain size likely records the transition from early continuous fountaining to late discrete Strombolian activity (observed and recorded on the 21 of June 2014, Fig. 2). This transition in activity is typical of many eruptions at PdF (Hibert et al., 2015). The reverse grading of the whole deposit (Figs. 3b and 3c) is thus not correlated with an increase in energy of the event, but with two different eruptive dynamics and fragmentation processes. The decrease in coarse ash, which correlates with the decrease in energy of the event, highlights the most efficient fragmentation process within the Hawaiian fountaining with respect to the slow gas ascent and explosion of the Strombolian activity. These conclusions are consistent with (i) the continuous and progressive decrease in intensity of Real time Seismic Amplitude Measurement recorded by the OVPF seismic network (unpublished data), and (ii) satellite derived TADR which suggest continuous decay of magma output rate after an initial short-lived intense phase (Coppola et al., 2017).

21

5.2 Interpretation of the different textural signatures and the meaning of the 4 typologies of clasts.

1) *Background on the texture of clasts from Hawaiian and Strombolian activities*

The first microtextural analysis of Hawaiian ejecta was performed by Cashman and Mangan (1994) and Mangan and Cashman (1996) on pyroclasts from 1984 to 1986 Pu'u 'Ō'ō fountainings. The authors defined two clast types: 1) 'scoria' consisting of closed-cell foam of ≤85% vesicularity, with round, undeformed, broadly-sized vesicles, and 2) 'reticulite', an open-cell polyhedral foam with ~1 μm thick vesicle walls with >95% vesicularity. They stated that the scoria to reticulite transition is a consequence of Ostwald ripening, where larger bubbles grow at the expense of smaller bubbles due to post-fragmentation expansion of clasts within the fountain. According to this model, scoria preserves textures closer to conditions at fragmentation, whereas continued vesiculation and clast expansion in the thermally-insulated core of the fountain results in reticulate. This model was confirmed at lava fountains at Etna (Polacci et al., 2006), Villarrica (Gurioli et al., 2008), Kīlauea Iki, (Stovall et al., 2011 and 2012), Mauna Ulu (Parcheta et al., 2013) and Al Madinah (Kawabata et al., 2015). These last authors also measured the connected and isolated porosity in the AD1256 Al-Madinah Hawaiian fountaining eruptions. They found that the reticulite-like textures from the central part of these very high fountains showed isolated vesicles in agreement with low shear rates and low viscosity melts, where bubbles may grow spherically and remain isolated. In contrast, at margins of the fountains, high shear may lead to stretching and mechanical coalescence of bubbles, forming the common, fluidal types of particles seen also in the deposits. They also stated that lower vesicularity and greater isolated porosity were found in some tephra interpreted as resulting from violent Strombolian eruptive phases.

The data that we found in our study of the typical activity of PdF agree only partially with all these interpretations. The reason is that we sampled and measured products of very weak Hawaiian to Strombolian activities. If we plot the approximate durations and masses of these events on the Houghton et al. (2016) diagram, the 2014 activity of PdF falls into the two fields for transient and fountaining activity, but at the base of the diagram. We here show for the first time that short lived and weak fountaining can preserve pyroclast textures that record magma ascent and fragmentation conditions before the explosions and also provide some information about the pre-eruptive storage conditions. The occurrence of time-variable ascent conditions is also reflected in the time evolution of eruptive dynamics, with the golden and

22

723   fluidal scoriae emitted from the low Hawaiian fountaining episodes and the spiny fragments

724   from the Strombolian-like explosions

725   *2) The four typologies of clasts and their distribution in space and in time in the 2014*

726   *eruption at PdF*

727   So, as described in 5.1, longitudinal variation in eruptive style along the fracture system

728   produces a spatial variability in the proportions of the four typologies of clasts. The

729   uppermost fractures (WF and UF, Fig. 1a) are characterized solely by fluidal fragments (Fig.

730   4b); they lack both the spiny and the golden components. In addition, these fluidal clasts are

731   the ones showing the smoothest surfaces (indicative of rapid quenching in a very hot

732   environment), low porosity values (between 50 to 77 vol. %, Fig. 6b), the highest content in

733   isolated vesicles (~ 30 vol. % Fig. 4c), and low vesicle numbers (3 to 5 x 10^6, Fig. 4b),

734   comparable to the spiny fragments. They have scarce mesocrysts (1-2 vol. % Table S3) and

735   very low amount of microcrysts of plagioclase and clinopyroxene (3 to 11 vol. %, Table S3).

736   These fluidal scoria fragments were emitted by short lived jets of magma, therefore they

737   underwent rapid quenching in a very hot environment that prevented any expansion or further

738   vesiculation and preserved a very high number of isolated vesicles (Fig. 6d). Syn-eruptive

739   crystallization was hindered by high ascent velocities in the dyke, due to the sudden release of

740   over-pressure in the shallow magma reservoir.

741   The four typology of clasts, golden pumice, fluidal scoria and the spiny fragments

742   (Fig. 4) were found associated only at the MV. The relative proportions of these four

743   typologies of clasts correlate with the eruptive dynamics. The golden lapilli and fluidal clasts

744   were in fact dominant in the Hawaiian, more energetic activity at the beginning of the

745   eruption (during the night between the 20 and the 21 of June 2014). In contrast, the spiny

746   fragments were dominant during the Strombolian activity, coinciding with the decreasing in

747   Mass Discharge Rate (MDR, early in the morning of the 21, Fig. 2 and Coppola et al., 2017).

748   The golden and fluidal fragments from the MV show the highest porosity (86 %, Fig. 6a),

749   variable proportions of isolated vesicles (Fig. 6c) and high, but variable, N_V numbers (Figs.

750   4a). They are also characterized by a uniform vesicle size population with clear evidence of

751   incipient expansion, especially in the fluidal fragments (Figs. 4a and 4b). From the

752   connectivity graph, there is a clear decrease in isolated vesicles with the increase in

753   vesicularity (Fig. 6c). The content in crystal, mostly formed by microcrysts of sodic

754   plagioclase (Fig. 10a) due to magma degassing during its ascent and decompression in the

755   conduit (Di Muro et al., 2015), is very low, especially in the golden pumice (up to 15 vol. %),

23

and slightly higher for the fluidal clasts (up to 23 vol. %). We interpret the golden fragments, at the MV, to be the fastest (low amount of microcrysts) and less degassed magma (high vesicularity coupled with high N_V), which experienced only a very short residence time in the magma transport system (dyke+vent), followed by the fluidal fragments. In contrast the spiny fragments, characterized by higher percentage of microcrysts and mesocrysts, by the lack of isolated vesicles, by the presence of coalescence signature and low N_V values (Figs. 4c and 4d), are indicative of an extensively degassed and cooled magma. The presence of the mesocrysts (that formed in the shallow reservoir) in the spiny fragments, and their slightly cooler temperature (Fig. 10b), strongly support this interpretation. The spiny fragments likely record the slowest ascent velocity and the longest residence time in the reservoir+dyke+vent system compared to the golden/fluidal counterpart. Therefore these fragments are associated with Strombolian events, and decreasing MDR, in agreement with their slower ascent that allows extensive syneruptive crystallization.

Among spiny fragments, the opaque ones are the densest, they lack a uniform glassy surface, and they are characterized by i) very high microcrysts content, ii) strong coalescence signature (Fig. 4d), iii) heterogeneous glass chemistry, and iv) mingling with hotter magma at the clast edges (Fig. 8a). All these features reveal the composite nature of these clasts. We interpret the spiny opaque as spiny glass fragments recycled inside the eruptive vent during the explosions, being the densest portion of the magma prone to fall back in the vent/fracture (Fig. 2b).

3) Degassing-driven versus cooling-driven crystallization

Syn-eruptive degassing is favoured by bubble connectivity/permeability (Figs. 6c and 6d) in the ascending magma, enhanced by syn-eruptive crystallisation in the conduit (especially microcrysts of plagioclase, Fig. 10a), even for magmas at low vesicularity. However, our dataset also supports the occurrence of magma stratification in the reservoir. Textural and petrological data demonstrate that the initial activity emitted a small volume of melt (represented by golden and large part of the fluidal fragments) with very scarce crystals. This crystal-poor melt was followed in time by the main volume of magma that contains a larger amount of mesocrysts (spiny clasts and lava). Lava flows represent the main volume emitted in the 2014 eruption. Mesocrysts are absent in the golden, scarce in the fluidal and more abundant in the spiny (Figs 4b, 4c and 4d) and lava (Fig. 4e) fragments and consist in an equal percentage of plagioclase and clinopyroxene and minor olivine. Their composition indicates

790   that they formed in the reservoir, as shown by their different composition in respect to the

791   microcrysts counterparts that formed during melt degassing in the conduit (Fig. 10a). Most

792   important, a large amount of microcrysts in lava formed in the reservoir as well during

793   magma cooling (Figure 10a). So, we have a range of crystallization conditions. The fact that

794   the lighter plagioclase are not concentrated in the upper and early erupted portion of the

795   reservoir can be due either to the fact that often they are locked in clusters with the

796   clinopyroxene or that this melt was expelled from the crystal-rich portion of the reservoir (see

797   Figure 10b). Water exsolution from the melt can result from its extensive crystallization,

798   which induces an increase in dissolved volatile content, up to saturation (second boiling) and

799   can drive melt-crystal separation.

800   In conclusion, the crystals in the 2014 fragments do reflect the shallow reservoir

801   conditions and the ascent degassing processes.

802

803   *4) Textural syn-eruptive versus post fragmentation modifications*

804

805   To prove that the 2014 vesiculation of the clasts have been not modified by post

806   fragmentation expansion process, following Stovall et al. (2011), we use a plot of vesicle-to-

807   melt ratio (V_G/V_L, after Gardner et al., 1996) and vesicle number density (N_V, Fig. 11). As

808   demonstrated by Stovall et al. (2011), addition of small bubbles leads to an increase in N_V and

809   only a slight increase in V_G/V_L. Bubble growth by some combination of diffusion and

810   decompression leads to an increase in V_G/V_L at constant N_V. N_V decreases while V_G/V_L

811   increases during bubble coalescence, whereas loss of bubbles via collapse or buoyant rise

812   leads to a reduction in both parameters. Intermediate trends on the diagram reflect

813   combinations of more than one of these processes. The pumice and the scoria from the MV of

814   PdF show the highest V_G/V_L, but also the highest Nv, suggesting preservation of small

815   vesicles and growth by some combination of diffusion and decompression. The presence of

816   the small vesicles and the lack of a strong coalescence/expansion signature confirm that the

817   weak PdF activity leads to only limited post-fragmentation expansion inside the hot portions

818   of the short-lived fountains. These data contrast with the data from the more energetic

819   fountaining events observed at Kilauea or elsewhere, where pre-eruptive information is

820   basically erased because pumice textures are dominated by expansion effects due to their

821   longer residence within the long-lived energetic fountaining. In contrast, the densest, spiny

822   scoriae and the scoria from the Fractures activity show the lowest values of Nv and V_G/V_L,

823   due to incipient coalescence and/or loose/lack of small bubbles.

25

According to previous works (listed above), the golden pumice of PdF should be derived from the central part of the fountains, but they do not show the strong post expansion signatures reported by other samples collected from more energetic Hawaiian fountainings (Fig. 11). It is interesting to note that the fluidal fragments at the MV are less smooth (Fig. 4), more vesiculated, and have a lower content of isolated vesicles than the fluidal scoria from the uppermost Fractures (Fig. 6). Therefore fluidal fragments at the 2014 MV could indeed represent clasts that have been partly modified during their residence in the external part of the fountains, while the golden samples could come from the central part (Stovall et al., 2011 and 2012). However, the slight differences in crystallinity and glass chemistry between the fluidal and golden fragments support the idea that each of these fragments has an imprint from the pre-fragmentation setting. In contrast, the spiny fragments from the MV and the fluidal fragments from the Fractures show low N_V and low V_G/V_L in agreement with loss of vesicles and coalescence. However, the presence of large numbers of isolated vesicles within the fluidal scoria from the Fractures agrees with their provenance from a fast hot ejection of relatively degassed magma (low N_V). In contrast the spiny fragments, especially because of the presence of abundant mesocrysts and increase in syneruptive microcrysts, are indicative of the slowest ascent velocity and extensively degassing and cooled magma. The spiny fragments are the most degassed, densest and the most crystal rich magma that was emitted during low-energy activity by Strombolian explosion, where recycling phenomena were also very frequent (Fig. 2f).

Our vesicle connectivity results are in full agreement with the recent review of Colombier et al. (2017b). According to these authors, connectivity values can be used as a useful tool to discriminate between the basaltic scoria from Hawaiian (fire fountaining) and Strombolian activity. The broad range in connectivity for pumice and scoria from fire fountaining is interpreted simply as being due to variations in the time available before quenching due to differences in location and residence time inside the fountain. The fluidal fragments from the WF are the richest in isolated vesicles because they are transported by very short lived hot lava jets. In contrast, the higher connectivity observed in scoria from Strombolian activity is probably related to their higher average crystallinity, and more extensive degassing prior to the eruption (Colombier et al., 2017b). The spiny surface of these Strombolian fragments is due to the fact that these weak explosions emit only a small solid mass fraction and the partially quenched dense clasts land quickly after a short cooling path through the surrounding atmosphere (e.g. Bombrun et al., 2015).

857　　　All the clast, from golden to spiny, are very permeable, independent on their
858　vesicularity, crystal content and/or of the presence of isolated vesicles. This is in agreement
859　with our interpretation that magma degasses during its ascent in the conduit and that promotes
860　microlite nucleation (see the sodic plagioclase, Fig. 10a) before magma fragmentation (see
861　also Di Muro et al. 2015 with the Pele's hairs and tears samples for the three 2008 eruptions).
862　Moreover, we always find that some of the spiny clasts (especially the opaque ones) are
863　slightly less permeable than the golden and fluidal ones, but not with a low permeability as we
864　would expect by their low vesicularity.

865　　　In conclusion, we can state that i) the crystals lower the percolation threshold and
866　stabilize permeable pathways and ii) this is true for the syn-eruptive sodic plagioclase that
867　favor an efficient degassing in the relatively crystal-rich magma, because of their low wet
868　angles that favor degassing against nucleation (Shea, 2017) and their aspect ratio (e.g. Spina
869　et al. 2016) iii) therefore permeability develops during vesiculation through bubble
870　coalescence, which allows efficient volatile transport through connected pathways and
871　relieves overpressure (Lindoo et al., 2017). Pervasive crystal networks also deform bubbles
872　and therefore enhance outgassing (Oppenheimer et al., 2015). Based on Saar et al. (2001)
873　crystals should start to affect the behavior of the exsolved volatile phase when they approach
874　20 vol. % (Lindoo et al., 2017). In our dataset, apart from the golden and part of fluidal, all
875　the other clasts do have microcrysts >20%. Our data completely support that slow
876　decompression rate allows more time for degassing-induced crystallization, which lowers the
877　vesicularity threshold at which bubbles start to connect.

878　　　Rapid re-annealing of pore throats between connected bubbles can happen due to short
879　melt relaxation times (Lindoo et al; 2016). This phenomenology could explain the high
880　amount of isolated vesicles in the fountaining samples. However, vesicle distributions of the
881　golden and fluidal fragments are almost perfect Gaussian curves, so it seems that if the
882　relaxation process happens it just merged perfectly with the expected vesicle distribution. In
883　contrast, coalescence and/or expansion (as we observe in the spiny fragments) do not fit the
884　curves (Fig. 4). In addition, we should expect that in crystal-poor fragments, due to melt
885　relaxing and pathway closure, the clasts became almost impermeable after quenching, as
886　revealed by some petrological experiments performed on crystal-poor basaltic magma
887　(Lindoo et al., 2016). In contrast, in high crystalline magmas, the presence of micro-crystals
888　increases viscosity thus preserving the coalesced textures (see Moitra et al., 2013). The
889　isolated vesicle-rich fragments of the 2014 PdF eruption are highly permeable, and are
890　characterized by variable ranges of porosity and numbers of vesicles (Fig.4 and Fig. 6d) that

891 seem more related to the pre-eruptive conditions than to the post relaxation of low-viscosity
892 melts. In the 2014 crystal-poor samples, the permeability increases rapidly once the
893 percolation threshold has been reached, and efficient degassing prevents bubble volumes from
894 expanding past the percolation threshold (Rust and Cashman 2011).

895   In conclusion, also the vesicles in the 2014 fragments do partly reflect the shallow
896 reservoir conditions and mostly the ascent degassing processes.

5.4 Integration between the physical and textural characteristics of the products and their geochemical signature: insight into the feeding system

899 According to Peltier et al. (2016), the June 2014 eruption emitted magma from a shallow
900 pressurized source located only 1.4-1.7 km below the volcano summit. Coppola et al. (2017)
901 suggest that the 2014 event was fed by a single shallow and small volume magma pocket
902 stored in the uppermost part of the PdF central plumbing system. All 2014 clasts show
903 homogeneous and evolved bulk compositions, irrespective of their textural features. June
904 2014 products are among the most evolved products erupted since at least 1998 and are
905 moderately evolved with respect to those emitted in 2010, just before the 2010-2014
906 quiescence. Bulk rock and melt inclusion data suggest that the 2014 evolved magma can be
907 produced by crystal fractionation during the long lasting (4.6 years) storage and cooling of the
908 magma injected and partly erupted in November 2009. The different types of scoria and
909 pumice emitted in 2014 show significant variations in glass composition (Fig. 8b) due to
910 variable degrees of micro-crystallization. In theory, microcrysts can reflect late stage (during
911 magma ascent and post-fragmentation) crystallization. In this case, their variable amount
912 within, for instance, the glassy and opaque parts of the spiny scoria might reflect slower
913 ascent velocity or longer residence time in the system (e.g. Hammer et al., 1999, Stovall et al.,
914 2012; Gurioli et al., 2014) in agreement also with the vesicle signature. However, the four
915 typologies of clasts differ also in terms of mesocryst content (from rare to 5 vol. % for the
916 golden and fluidal and 14-23 vol. % for the glassy spiny and spiny opaque, respectively).
917 Equilibrium plagioclase-melt pairs record an almost constant and moderate dissolved water
918 content, intermediate between that expected for melts sitting in the main shallow reservoir
919 (located close to sea level) and the degassed matrix of lavas. Dissolved water contents are
920 thus consistent with pre-eruptive magma water degassing during its storage at shallow level,
921 as suggested by geophysical data, and suggest that the plagioclase mesocrysts and some of the
922 microcrysts in the spiny scoria and in the lava grew during magma storage (Fig. 10a). Melt

28

923   composition records a potential pre-eruptive thermal gradient of ~30 °C between the hotter

924   (pumice and fluidal) and the cooler (spiny) magma (Fig. 10b).

925   Tait et al. (1989) suggest that magma evolution can lead to oversaturation of volatile

926   species within a shallow reservoir and trigger a volcanic eruption. At PdF, the golden and the

927   fluidal clasts might represent the portion of magma located at the top of the shallow reservoir

928   and enriched in bubbles of water rich fluids, released by the cooler, more crystallized and

929   more degassed "spiny-lava" magma (Fig. 10b). The small volume of magma, its constant bulk

930   composition and the very small inflation recorded prior to the eruption (Fig. 1d) could be

931   consistent with an internal source of over-pressure related to volatile exsolution. Larger

932   inflation rates over a broader area are expected when shallow reservoir pressurization is

933   related to a new magma input from a deeper source. Slight baseline extensions both on distal

934   and proximal sites suggest that magma transfer towards shallower crustal levels started short

935   before (11 days) the final magma eruption. Geochemical data do not support the occurrence of

936   a new magma input in the degassed and cooled 2014 reservoir. We can thus speculate that

937   stress field change related to progressive deep magma transfer has promoted volatile

938   exsolution, melt-crystal separation and melt expansion in the shallow reservoir. Textural

939   heterogeneity of the 2014 products partly reflects a pre-eruptive physical gradient recorded by

940   the variability in crystal and bubble contents in the shallow reservoir feeding this eruption.

941   The golden and fluidal fragments are the bubble richer and hotter portion of the melt. The

942   spiny fragments are the degassed and cooler portion of the reservoir, whose progressive

943   tapping led to a decrease in explosive intensity (from fountaining to Strombolian activity).

944   Our results are also consistent with processes of mechanical reservoirs/dyke stratification, as

945   observed by Menand and Phillips (2007). As explained earlier, magma ascent promoted

946   syneruptive degassing induced crystallization. The spiny opaque clasts can be considered as

947   being recycled material that fell back into the system. Accumulation of olivine crystals out of

948   equilibrium with the host magma produces minor variations in mesocryst contents as

949   observed within the same type of clasts sampled at different times/locations during the

950   eruption, with the scoria from the WF and early erupted lava being the ones with the lowest

951   amount of olivine (Table S4 and Fig. 7b). Again, this temporal variation supports an increase

952   in large heavy crystals within the most degassed magma emitted toward the end of activity,

953   further suggesting that it corresponds to the lower part of the reservoir.

954   Our dataset permits us to propose that the 2014 eruption was fed by a physically zoned

955   magma reservoir. The low-density, crystal-poor, bubble-rich magma located in the upper part

956   of the storage system, ascended first, rapidly and fed the early, more energetic phase, the

29

957   Hawaiian fountaining. This low-density magma is not more evolved than the spiny one (same

958   bulk compositions) and it is not necessarily richer in dissolved volatile amounts; it is just

959   poorer in crystal and richer in bubbles. Second boiling, possibly triggered a few days before

960   the eruption by stress field change, is responsible of the extraction of bubble rich melt from a

961   crystal-rich network. This last one will represent the main volume of the erupted lava. Fast

962   ascent of the foam hinders its crystallization and preserves high number of vesicles, high

963   vesicularity and it is only little modified by post-fragmentation expansion. Decrease in initial

964   overpressure translates in a progressive decrease in magma ascent rate and output rate (e.g.

965   Coppola et al., 2017 and references therein). Nucleation of microcrysts is enhanced in melt

966   ascending with lower speed and is mostly related to syneruptive degassing (for the spiny). The

967   larger volume (dense lava) corresponds to crystallized and less vesiculated magma which

968   experiences a slow ascent in the dyke and even further micro-crystallisation during its

969   subaerial emplacement.

970   Melt inclusion results allow us to confirm the involvement of a single and only slightly

971   heterogeneous magma source in 2014, related to cooling and fractional crystallisation of an

972   older magma batch (November 2009). Interestingly, this latter short lived summit eruption

973   was also characterized by the same large textural range of pyroclastic products found in 2014

974   in spite of its more mafic composition.

975   This suggests that bubble accumulation and source pressurisation is highly dependent

976   on the shallow storage depth, which facilitates rapid water exsolution (Di Muro et al., 2016),

977   and it is not necessarily the outcome of slow magma cooling and differentiation (Tait et al.,

978   1989).

979   **6. Proposed model for the 2014 eruption and conclusions**

980   In this paper we show that textural and petro-chemical study of the eruptive products can be

981   used to characterize the on-going activity at PdF and to constrain both the trigger and the

982   evolution of short-lived and small-volume eruptions. This approach is extremely valuable in i)

983   understanding processes that lead to an eruption which was preceded by short-lived and

984   elusive precursors, and ii) in reconstructing the time evolution of eruptive dynamics in an

985   eruption with poor direct observations.

986   Following the sketch in Figure 12, we infer that residual magma from the 2009

987   eruption ponding at shallow levels experienced long-lasting cooling and crystallization (Fig.

988   12a). Between 2010 and 2014 the volcano progressively deflated (Fig. 12b) possibly because

989 of magma degassing and cooling, facilitated by the shallow depth of the reservoir. During this
990 phase mesocrysts and some microcrysts formed (Figs. 4e and 10a).

991 The occurrence of deep (>10 km bsl) lateral magma transfer since March-April 2014
992 has been inferred by Boudoire et al., (2017) on the basis of deep (mantle level) seismic
993 swarms and increase in soil CO_2 emissions on the distal western volcano flank. The incipit of
994 magma transfer towards shallower crustal levels is potentially recorded by subtle volcano
995 inflation about 11 days before the June 2014 eruptions (Figs. 1d and 12c). We suspect that
996 these deep processes can have progressively modified the shallow crustal stress field and
997 favoured magma vesiculation and melt-crystal separation. Second boiling could thus have
998 over-pressured the shallow seated reservoir and triggered magma ascent (Fig. 12c).

999 Without this deep magma transfers we believe that the small reservoir activated in
1000 2014 would have cooled down completely to form an intrusion (as suggested by the pervasive
1001 crystallization of the lava, one of the densest emitted from 2014 to 2017, Harris et al. 2017).
1002 The 2014 event represented instead the first of a long series of eruptions, whose magmas
1003 became progressively less evolved in time (Coppola et al., 2017). In this scenario the trigger
1004 mechanisms of 2014 activity are both internal and external in the sense that the small shallow
1005 reservoir hosting cooled magma permitted to create the conditions favourable to a second
1006 boiling (Fig. 12c, and Tait et al., 1989). The second boiling was likely triggered by an almost
1007 undetectable stress field change, and was favoured by the shallow storage pressure of the
1008 magma (Fig. 12c) that promoted fast water exsolution and rapid magma response to external
1009 triggers. The second boiling possibly contributed to the inflation registered 11 days before the
1010 eruption at 1.4-1.7 km (Fig. 12c) caused both by magma expansion and transfer of hot fluids
1011 to the hydrothermal system (Lénat et al., 2011).

1012 Our data permit to exclude (i) new magma input and/or fluid inputs (CO2-rich fluids)
1013 from deep magmatic levels to trigger the June 2014 eruption. We also exclude (ii) heating and
1014 enhanced convection of the shallow magma reservoir (due to heat diffusion without fluid or
1015 mass transfer), because this process is very slow. Furthermore, the 2014 minerals do not
1016 record evidences of magma heating. We can exclude equally (iii) deformation of the volcanic
1017 edifice and decompression of the magma reservoir and/or hydrothermal system due to flank
1018 sliding because geodetic data show no evidence of flank sliding able to produce stress change
1019 in the hydrothermal and magmatic system. Geophysical and geochemical data have permitted
1020 to track vertical magma and fluid transfer below the volcano summit in April 2015, that is
1021 about one year after the early deep lateral magma transfer (Peltier et al., 2016). Deep
1022 processes are difficult to detect for any monitoring network.

31

1023   We conclude that the overpressure, caused by the second boiling, triggered the

1024 eruption. The occurrence of a hydrous almost pure melt at shallow depth permitted its fast

1025 vesiculation upon ascent towards the surface. In turn, fast ascent of the foam (Fig. 12d)

1026 hindered its crystallization and preserved high number of vesicles. Decrease in initial

1027 overpressure translated in a progressive decrease in magma ascent rate and output rate (e.g.

1028 Coppola et al., 2017 and references therein) and a temporal transition from Hawaiian activity

1029 to Strombolian activity (Fig. 12 d). Nucleation of microcrysts was enhanced in melt ascending

1030 with lower speed and in turn this syn-eruptive crystallization favoured bubble

1031 connectivity/permeability in the ascending magma, even for magma at low vesicularity. The

1032 largest volume (dense lava) corresponds to highly-crystallized and degassed magma already

1033 in the reservoir, that experienced a slower ascent in the dyke and even further micro-

1034 crystallisation during its subaerial emplacement.

1035   The texture of the products allowed us to follow the dynamic evolution of the system

1036 in space, from smooth fluidal scoria emitted from rapid jet of lava at the fractures, to a more

1037 stable activity at the MV, and in time. At the MV, in fact, we observed the transition from the

1038 golden and fluidal fragments emitted from Hawaiian fountaining, at the peak of the intensity

1039 of the eruption, to the spiny fragments, emitted from a declining Strombolian activity at the

1040 end of the eruption.

1041   Therefore we here show for the first time that short lived and weak Hawaiian

1042 fountaining and Strombolian events can preserve pyroclast textures that can be considered a

1043 valid approximation to shallow reservoir conditions and ascent degassing processes before the

1044 explosions and correlate to the eruptive dynamics as well.

1045   To conclude, these results highlight the importance of petrological monitoring, which

1046 can provide complementary information regarding the ongoing volcanic activity to other

1047 geophysical and geochemical monitoring tools commonly used on volcanoes.

1055

1056 **References list**

1057 Albarède, F., and V. Tamagnan (1988), Modelling the recent geochemical evolution of the

1058 Piton de la Fournaise volcano, Réunion island, 1931-1986, *J. Petrol., 29*, 997-1030.

1059 Albarède, F., B. Luais, G. Fitton, M.P. Semet, E. Kaminski, B.G.J Upton, P. Bachèlery, and

1060 J.L. Cheminée (1997), The geo-chemical regimes of Piton de la Fournaise Volcano Réunion.

1061 during the last 530,000 years, *J. Petrol., 38*, 171–201.

1062 Andronico, D., M.D. Lo Castro, M. Sciotto, and L. Spina (2013a), The 2010 ash emissions at

1063 the summit craters of Mt Etna: relationship with seismo-acoustic signals, *J. Geophys. Res.,*

1064 *118*, 51–70, doi:10.1029/2012JB009895.

1065 Andronico, D., J. Taddeucci, A. Cristaldi, L. Miraglia, P. Scarlato, and M. Gaeta (2013b), The

1066 15 March 2007 paroxysm of Stromboli: video-image analysis, and textural and compositional

1067 features of the erupted deposit, Bull. Volcanol., 75, 733, doi:10.1007/s00445-013-0733-2.

1068 Andronico, D., S. Scollo, M.D. Lo Castro, A. Cristaldi, L. Lodato, and J. Taddeucci (2014),

1069 Eruption dynamics and tephra dispersal from the 24 November 2006 paroxysm at South-East

1070 Crater, Mt Etna, Italy, *J. Volcanol. Geotherm. Res., 274*, 78–91,

1071 doi:10.1016/j.jvolgeores.2014.01.009.

1072 Bachèlery, P., J.F. Lénat, A. Di Muro, and L. Michon (2016), Active Volcanoes of the

1073 Southwest Indian Ocean: Piton de la Fournaise and Karthala. Active Volcanoes of the World.

1074 Springer-Verlag, Berlin and Heidelberg, 1-428, DOI 10.1007/978-3-642-31395-0_12.

1075 Boivin, P., and P. Bachèlery (2009), Petrology of 1977 to 1998 eruptions of Piton de la

1076 Fournaise, La Réunion Island, *J. Volcanol. Geotherm. Res., 184*, 109–125.

1077 Bombrun, M., A. Harris, L. Gurioli, J. Battaglia and V. Barra (2015), Anatomy of a

1078 strombolian eruption: inferences from particle data recorded with thermal video, *J. Geophys.*

1079 *Res., 120*(4):2367-2387. DOI.10.1002/2014BO11556.

1080 Boudoire, G., M. Liuzzo, A. Di Muro, V. Ferrazzini, L. Michon, F. Grassa, A. Derrien, N.

1081 Villeneuve, A. Bourdeu, C. Brunet, G. Giudice, and S. Gurrieri (2017), Investigating the

1082 deepest part of a volcano plumbing system: evidence for an active magma path below the

33

1083 western flank of Piton de la Fournaise (La Réunion Island), *J. Volcanol. Geotherm. Res.*, doi:
1084 10.1016/j.jvolgeores.2017.05.026.

1085 Brenguier, F., P. Kowalski, T. Staudacher, V. Ferrazzini, F. Lauret, P. Boissier, A. Lemarchand,
1086 C. Pequegnat, O. Meric, C. Pardo, A. Peltier, S. Tait, N.M. Shapiro, M. Campillo, and A. Di
1087 Muro (2012), First Results from the UnderVolc High Resolution Seismic and GPS network
1088 deployed on Piton de la Fournaise Volcano, *Seismo. Res. Lett. 83*(7),
1089 doi:10.1785/gssrl.83.1.97.

1090 Brugier, Y.A. (2016), Magmatologie du Piton de la Fournaise (Ile de la Réunion): approche
1091 volcanologique, pétrologique et expérimentale. Sciences de la Terre. Université d'Orléans,
1092 NNT: 2016ORLE2007, pp. 251.

1093 Bureau, H., F. Pineau, N. Métrich, P.M. Semet, and M. Javoy (1998a), A melt and fluid
1094 inclusion study of the gas phase at Piton de la Fournaise volcano (Reunion Island), *Chem.*
1095 *Geol. 147*, 115–130.

1096 Bureau, H., N. Métrich, F. Pineau, and M.P. Semet (1998b), Magma-conduit interaction at
1097 Piton de la Fournaise volcano (Réunion Island): a melt and fluid inclusion study, *J. Volcanol.*
1098 *Geotherm. Res. 84*, 39–60.

1099 Carey, R.J., M. Manga, W. Degruyter, D. Swanson, B. Houghton, T. Orr, and M. Patrick
1100 (2012), Externally triggered renewed bubble nucleation in basaltic magma: the 12 October
1101 2008 eruption at Halema'uma'u Overlook vent, Kīlauea, Hawai'i, USA, *J. Geophys. Res.,*
1102 *117*, B11202. doi:10.1029/2012JB009496.

1103 Carey, R.J., M. Manga, W. Degruyter, H. Gonnermann, D. Swanson D, B. Houghton, T. Orr,
1104 and M. Patrick (2013), Convection in a volcanic conduit recorded by bubbles, *Geology, 41*(4),
1105 395–398.

1106 Cashman, K.V., and M.T. Mangan (1994) Physical aspects of magmatic degassing II:
1107 constraints on vesiculation processes from textural studies of eruptive products, In: Carroll
1108 MR, Holloway JR (eds) Volatiles in magmas, Reviews in mineralogy. *Miner. Soc. Am.,*
1109 Fredricksberg, pp 447–478.

1110 Clocchiatti, R., A. Havette, and P. Nativel (1979), Relations pétrogénétiques entre les basaltes
1111 transitionnels et les océanites du Piton de la Fournaise (Ile de La Réunion, océan Indien) à

1112   partir e la composition chimique des inclusions vitreuses des olivines et des spinelles, *Bull.*

1113   *Minér., 102*, 511–525.

1114   Colombier, M., L. Gurioli, T.H. Druitt, T. Shea, P. Boivin, D. Miallier, and N. Cluzel (2017a),

1115   Textural evolution of magma during the 9.4-ka trachytic explosive eruption at Kilian Volcano,

1116   Chaîne des Puys, France, *Bull. Volcanol., 79*(2), 1-24. doi:10.1007/s00445-017-1099-7.

1117   Colombier, M., F.B. Wadsworth, L. Gurioli, B. Scheu, U. Kueppers, A. Di Muro, and D.B.

1118   Dingwel (2017b), The evolution of pore connectivity in volcanic rocks, *Earth Planet. Sci.*

1119   *Lett., 462*, 99-109. DOI: 10.1016/j.epsl.2017.01.011.

1120   Colò, L., M. Ripepe, D.R. Baker, and M. Polacci (2010), Magma vesiculation and infrasonic

1121   activity at Stromboli open conduit volcano, *Earth Planet. Sc. Lett. 292*(3–4):274–280.

1122   Coppola, D., N. Villeneuve, A. Di Muro, V. Ferrazzini, A. Peltier, M. Favalli, P. Bachèlery, L.

1123   Gurioli, A. Harris, S. Moune, I. Vlastélic, B. Galle, S. Arellano, and A. Aiuppa (2017), A

1124   Shallow system rejuvenation and magma discharge trends at Piton de la Fournaise volcano

1125   (La Réunion Island), *Earth Planet. Sci. Lett. 463*, 13-24.

1126   Corsaro, R., and L. Miraglia (2014), The transition from summit to flank activity at Mt. Etna,

1127   Sicily (Italy): Inferences from the petrology of products erupted in 2007–2009, *J. Volcanol.*

1128   *Geother. Res., 275*, 51– 60.

1129   Darcy, H. (1856) Les Fontaines Publiques de la Ville de Dijon, Dalmont, Paris.

1130   Di Muro, A., Métrich, N., Vergani, D., Rosi, M., Armienti, P., Fougeroux, T., Deloule, E.,

1131   Arienzo, I., Civetta, L. (2014), The shallow plumbing system of Piton de la Fournaise Volcano

1132   (La Réunion Island, Indian Ocean) revealed by the major 2007 caldera forming eruption, *J.*

1133   *Petrol., 55*, 1287-1315.

1134   Di Muro, A., T. Staudacher, V. Ferrazzini, N. Métrich, P. Besson, C. Garofalo, and B.

1135   Villemant (2015), Shallow magma storage at Piton de la Fournaise volcano after 2007 summit

1136   caldera collapse tracked in Pele's hairs, chap 9 of Carey, R. J., V. Cayol, M. P. Poland, and D.

1137   Weis (eds.), Hawaiian Volcanoes: From Source to Surface, *American Geophysical Union*

1138   *Monograph 208*, pp 189–212, doi:10.1002/9781118872079.ch9.

1139 Di Muro, A., N. Métrich, P.Allard, A. Aiuppa, M. Burton, B. Galle, and T. Staudacher (2016),

1140 Magma degassing at Piton de la Fournaise volcano, Active Volcanoes of the World, series,

1141 Springer, Bachelery, P., Lenat, J.F, Di Muro, A., Michon L., Editors. Pg. 203-222.

1142 DYNVOLC Database (2017) Observatoire de Physique du Globe de Clermont-Ferrand,

1143 Aubière,   France.   DOI:10.25519/DYNVOLC-Database.   Online   access:

1144 http://dx.doi.org/10.25519/DYNVOLC-Database

1145 Eychenne, J., B.F. Houghton, D.A. Swanson, R.J. Carey, and L; Swavely (2015), Dynamics of

1146 an open basaltic magma system: the 2008 activity of the Halemaʻumaʻu Overlook vent,

1147 Kīlauea Caldera. *Earth Planet. Sci. Lett., 409*, 49–60.

1148 Famin, V., B. Welsch, S. Okumura, P. Bachèlery, and S. Nakashima (2009), Three

1149 differentiation stages of a single magma at Piton de la Fournaise (Réunion hotspot). *Geoch.*

1150 *Geoph. Geos. 10*, Q01007. doi:10. 1029/2008GC002015.

1151 Fisk, M.R., B.G.J Upton, C.E. Ford, and W.M. White (1988), Geochemical and experimental

1152 study of the genesis of magmas of Reunion island, Indian Ocean, *J. Geophys. Res., 93*, 4933-

1153 4950.

1154 Forchheimer, P. (1901) Wasserbewegung durch Boden, Z. Ver. Dtsch. Ing. 45:1781–1788.

1155 Formenti, Y, and T.H. Druitt (2003), Vesicle connectivity in pyroclasts and implications for

1156 the fluidisation of fountain-collapse pyroclastic flows, Montserrat (West Indies), *Earth Planet.*

1157 *Sci. Lett., 214*, 561–574.

1158 Gardner, J.E., R.M.E. Thomas, C. Jaupart, and S. Tait (1996), Fragmentation of magma

1159 during Plinian volcanic eruptions, *Bull. Volcanol., 58*, 144–162.

1160 Giachetti, T., T.H. Druitt, A. Burgisser, L. Arbaret, and C. Galven (2010), Bubble nucleation

1161 and growth during the 1997 Vulcanian explosions of Soufrière Hills Volcano, Montserrat, *J.*

1162 *Volcanol. Geotherm. Res., 193*(3–4):215–231. doi:10.1016/j.jvolgeores.2010.04.001.

1163 Gonnermann, H.M., and M. Manga (2013) Dynamics of magma ascent in the volcanic

1164 conduit. In: Fagents, S.A., Gregg, T.K.P., Lopes, R.M.C. (Eds.), Modeling Volcanic Processes:

1165 The Physics and Mathematics of Volcanism. Cambridge University Press, Cambridge.

Gurioli, L., A.J.L. Harris, B.F. Houghton, M. Polacci, and M. Ripepe (2008) Textural and geophysical characterization of explosive basaltic activity at Villarrica volcano, *J. Geophys. Res., 113*, B08206. doi:10.1029/2007JB005328

Gurioli, L., A.J.L. Harris, L. Colo, J. Bernard, M. Favalli, M. Ripepe, and D. Andronico (2013), Classification, landing distribution and associated flight parameters for a bomb field emplaced during a single major explosion at Stromboli, Italy, *Geology, 41*, 559-562, DOI 10.1130/G33967.1.

Gurioli, L., L. Colo', A.J. Bollasina, A.J.L. Harris, A. Whittington, and M. Ripepe (2014), Dynamics of strombolian explosions: inferences from inferences from field and laboratory studies of erupted bombs from Stromboli volcano, *J. Geophys. Res., 119*(1), DOI:10.1002/2013JB010355.

Gurioli, L., D. Andronico, P. Bachelery, H. Balcone-Boissard, J. Battaglia, G. Boudon, A. Burgisser, S.B. M.R. Burton, K. Cashman, S. Cichy, R. Cioni, A. Di Muro, L. Dominguez, C. D'Oriano, T. Druitt, A.J.L Harris, M. Hort, K. Kelfoun, J.C. Komorowski, U. Kueppers, J.L. Le Pennec, T. Menand, R. Paris, L. Pioli, M. Pistolesi, M. Polacci, M. Pompilio, M. Ripepe, O. Roche, E. Rose-Koga, A. Rust, L. Scharff, F. Schiavi, R. Sulpizio, J. Taddeucci, and T. Thordarson (2015), MeMoVolc consensual document: a review of cross-disciplinary approaches to characterizing small explosive magmatic eruptions, *Bull. Volcanol., 77*, 49. DOI: 10.1007/s00445-015-0935-x.

Hammer, J.E., K.V. Cashman, R.P. Hoblitt, and S. Newman (1999) Degassing and microlite crystallization during pre-climactic events of the 1991 eruption of Mt. Pinatubo, Philippines, *Bull. Volcanol. 60*, 355–380.

Harris, A.J.L., N. Villeneuve, A. Di Muro, V. Ferrazzini, A. Peltier, D. Coppola, M. Favalli, P. Bachèlery, J.-L. Foger, L. Gurioli, S. Moune, I. Vlastélic, B. Galle, and S. Arellano (2017), Effusive Crises at Piton de la Fournaise 2014-2015: A Review of a Multi-National Response Model, *Applied Volcanology, 6,* 11, DOI 10.1186/s13617-017-0062-9

Helz, R.T., and C.R. Thornber (1987), Geothermometry of Kilauea Iki lava lake, Hawaii, *Bull. Volcanol., 49*, 651–668.

Hibert, C, A. Mangeney, M. Polacci, A. Di Muro, S. Vergniolle, V. Ferrazzini, B. Taisne, M. Burton, T. Dewez, G. Grandjean, A. Dupont, T. Staudacher, F. Brenguier, N.M. Shapiro, P.

1196　Kowalski, P. Boissier, P. Catherine, and F. Lauret (2015), Multidisciplinary monitoring of the

1197　January 2010 eruption of Piton de la Fournaise volcano, La Réunion island, *J. Geophis. Res.,*

1198　*120*(5), 3026-3047

1199　Higgins M.-D. (2000). Measurement of crystal size distributions, *American Mineralogist*, 85,

1200　1105-1116.

1201　Houghton, B.F., and C.J.N. Wilson (1989), A vesicularity index for pyroclastic deposits, *Bull.*

1202　*Volcanol., 51*, 451–462. doi:10.1007/BF01078811

1203　Houghton, B.F., D.A. Swanson, R.J. Carey, J Rausch., and A.J Sutton (2011), Pigeonholing

1204　pyroclasts, insights from the 19 March 2008 explosive eruption of Kīlauea volcano,

1205　*Geology,39*, 263–266, doi:10.1130/G31509.1.

1206　Houghton, B.F., D.A. Swanson, J. Rausch, R.J. Carey, Fagents S.A., and T.R. Orr (2013),

1207　Pushing the volcanic explosivity index to its limit and beyond: constraints from exceptionally

1208　weak explosive eruptions at Kılauea in 2008, *Geology, 41*(6):627–630

1209　Houghton, B.F., J. Taddeucci, D. Andronico, H.M. Gonnermann, M. Pistolesi, M.R. Patrick,

1210　T.R. Orr, D.A. Swanson, M.Edmonds, D. Gaudin, R.J. Carey and P. Scarlato (2016), Stronger

1211　or longer: Discriminating between Hawaiian and Strombolian eruption styles, *Geology* doi:

1212　10.1130/G37423.1

1213　Inman, D.L. (1952) Measures for describing the size distribution of sediments, *J. Sed. Petrol.,*

1214　*22*, 125–145.

1215　Kahl, M., S.Chakraborty, M. Pompilio, and F. Costa (2015), Constraints on the nature and

1216　evolution of the magma plumbing system of Mt. Etna Volcano (1991–2008) from a combined

1217　thermodynamic and kinetic modelling of the compositional record of minerals, *J.Petrol., 56*,

1218　2025–2068, doi:10.1093/petrology/egv063.

1219　Kawabata, E., S.J. Cronin, M.S. Bebbington, M.R.H. Moufti, N. El-Masry, and T. Wang

1220　(2015), Identifying multiple eruption phases from a compound tephra blanket: an example of

1221　the AD1256 Al-Madinah eruption, Saudi Arabia, *Bull. Volcanol., 77*, 6 DOI 10.1007/s00445-

1222　014-0890-y.

1223　Lange, R.A., H.M. Frey, and J. Hector (2009), A thermodynamic model for the plagioclase-

1224　liquid hygrometer/thermometer, *Am. Mineral., 94*, 494–506.

38

Lautze, N., J. Taddeucci, D. Andronico, C. Cannata, L. Tornetta, P. Scarlato, B. Houghton, and D. Lo Castro (2012), SEM-based methods for the analysis of basaltic ash from weak explosive activity at Etna in 2006 and the 2007 eruptive crisis at Stromboli, *Phys. Chem. Earth 45*,46, 113–127, doi:10.1016/j.pce.2011.02.001.

Leduc, L., L. Gurioli, A.J.L. Harris, L. Colo', and E. Rose-Koga (2015), Types and mechanisms of strombolian explosions: characterization of a gas-dominated explosion at Stromboli, *Bull. Volcanol., 77*, 8, DOI: 10.1007/s00445-014-0888-5

Lénat, J.-F., P. Bachèlery, and A. Peltier (2011), The interplay between collapse structures, hydrothermal systems and magma intrusions: the case of the central area of Piton de la Fournaise volcano, *Bull. Volc.* doi:10.1007/s00445-011-0535-3

Lénat, E.F., P.B. Bachelery, and O. Merle (2012), Anatomy of Piton de la Fournaise volcano (La Réunion, Indian Ocean), *Bull. Volcanol. 74*, 1945–1961.

Lengliné, O, Z. Duputel, and V. Ferrazzini (2016), Uncovering the hidden signature of a magmatic recharge at Piton de la Fournaise volcano using small earthquakes, *Geophys. Res. Lett., 43*, doi: 10.1002/2016GL068383

Lindoo, A., J.F. Larsen, K.V. Cashman, A.L. Dunn, and O.K Neill (2016), An experimental study of permeability development as a function of crystal-free melt viscosity, *Earth Planet. Sci. Lett., 435*, 45–54, doi: 10 .1016 /j .epsl .2015 .11 .035.

Lindoo, A., J.F. Larsen, K.V. Cashman, and J. Oppenheimer (2017), Crystal controls on permeability development and degassing in basaltic andesite magma, *Geology, 45*(9), p. 831-834.

Liuzzo, M., Di Muro, A., Giudice, G., Michon, L., Ferrazzini, V., and Gurrieri, S. (2015), New evidence of CO2 degassing anomalies on the Piton de la Fournaise volcano and the link with volcano tectonic structures Geochemistry, Geophysics, Geosystems, 16, doi:10.1002/ 2015GC006032.

Mangan, M.T., and K.V. Cashman (1996), The structure of basaltic scoria and reticulite and inferences for vesiculation, foam formation, and fragmentation in lava fountains. *J. Volcanol. Geotherm. Res., 73*, 1–18.

1253 Menand, T., and J.C. Phillips (2007), Gas segregation in dykes and sills. *J. Volcanol. Geother.*
1254 *Res.*, *159*(4), 393–408. https://doi.org/10.1016/j.jvolgeores.2006.08.003.

1255 Michon, L., A. Di Muro, N. Villeneuve, C. Saint-Marc, P. Fadda, and F. Manta (2013),
1256 Explosive activity of the summit cone of Piton de la Fournaise volcano (La Réunion Island): a
1257 historical and geological review, *J. Volcanol. Geotherm. Res. 263*, 117-133.

1258 Moitra, P., H.M. Gonnermann, B.F. Houghton, and T. Giachetti (2013), Relating vesicle
1259 shapes in pyroclasts to eruption styles, *Bull. Volcanol.* 75, 691. doi:10.1007/s00445-013-0691-
1260 8

1261 Morgan D.J., and D.A. Jerram (2006), On estimating crystal shape for crystal size distribution
1262 analysis, *J. Volc. Geotherm. Res., 154*, 1–7.

1263 Moune, S., O. Sigmarsson, P. Schiano, T. Thordarson, and J.K. Keiding (2012), Melt
1264 inclusion constraints on the magma source of Eyjafjallajökull 2010 flank eruption, *J.*
1265 *Geophys. Res., 117*, B00C07, doi:10.1029/2011jb008718.

1266 Morandi, A., C. Principe, A. Di Muro, G. Leroi, L. Michon, and P. Bachèlery (2016), Pre-
1267 historic explosive activity at Piton de la Fournaise volcano. In: Bachèlery P, Lénat JF, Di
1268 Muro A, Michon L (eds) Active Volcanoes of the Southwest Indian Ocean: Piton de la
1269 Fournaise and Karthala. Active Volcanoes of the World. Springer-Verlag, Berlin and
1270 Heidelberg, pp 107–138

1271 Óladóttir, B., O. Sigmarsson, G. Larsen, and J.-L. Devidal (2011), Provenance of basaltic
1272 tephra from Vatnajökull subglacial volcanoes, Iceland, as determined by major- and trace-
1273 element analyses, *Holocene, 21*, 1037–1048, doi:10.1177/0959683611400456.

1274 Oppenheimer, J., A.C. Rust, K.V. Cashman, and B. Sandnes (2015), Gas migration regimes
1275 and outgassing in particle-rich suspensions, *Frontiers in Physics, 3*, 1–13, doi: 10 .3389 /fphy
1276 .2015 .00060.

1277 Ort, M.H., A. Di Muro, L. Michon, and P. Bachèlery (2016), Explosive eruptions from the
1278 interaction of magmatic and hydrothermal systems during flank extension: the Bellecombe
1279 Tephra of Piton de La Fournaise (La Réunion Island), *Bull. Volcanol. 78*, 5,
1280 doi:10.1007/s00445-015-0998-8.

1281 Papale P., R. Moretti, and D. Barbato (2006), The compositional dependence of the saturation
1282 surface of H2O + CO2 fluids in silicate melts, *Chemical Geology*, 229, 1/3, 78-95,
1283 doi:10.1016/j.chemgeo.2006.01.013.

1284 Parcheta, C.E., B.F. Houghton, and D.A. Swanson (2013), Contrasting patterns of vesiculation
1285 in low, intermediate, and high Hawaiian fountains: a case study of the 1969 Mauna Ulu
1286 eruption, *J. Volcanol. Geotherm. Res., 255*, 79–89

1287 Peltier, A., P. Bachèlery, and T. Staudacher (2009), Magma transport and storage at Piton de la
1288 Fournaise (La Réunion) between 1972 and 2007: A review of geophysical and geochemical
1289 data. *J. Volcanol.Geother. Res., 184,* 93-108.

1290 Peltier, A., F. Beauducel, N. Villeneuve, V. Ferrazzini, A. Di Muro, A. Aiuppa, A. Derrien, K.
1291 Jourde, and B. Taisne (2016), Deep fluid transfer evidenced by surface deformation during the
1292 2014–2015 unrest at Piton de la Fournaise volcano, *J. Volcanol. Geotherm. Res., 321*, 140–
1293 148. http://dx.doi.org/10.1016/j.jvolgeores.2016.04.031.

1294 Polacci, M., R. Corsaro, and D. Andronico (2006), Coupled textural and compositional
1295 characterization of basaltic scoria: insights into the transition from Strombolian to fire
1296 fountain activity at Mount Etna, Italy, *Geology, 34*(3), 201–204. doi:10.1130/G223181.1.

1297 Polacci, M., C. Bouvet de Maisonneuve, D. Giordano, M. Piochi, L. Mancini L., W.
1298 Degruyter, and O. Bachmanng (2014), Permeability measurements of Campi Flegrei
1299 pyroclastic products: an example from the Campanian Ignimbrite and Monte Nuovo
1300 eruptions. *J. Volcanol. Geotherm. Res. 272*, 16–22.

1301 Putirka, K.D. (2008), Thermometers and barometers for volcanic systems, *Rev. Mineral.*
1302 *Geochem. 69*, 61-120.

1303 Reynolds, O. (1900) Papers on Mechanical and Physical Subjects, Cambridge University
1304 Press.

1305 Roeder, P., E. Gofton, and C. Thornber (2006), Cotectic proportions of olivine and spinel in
1306 olivine-tholeiitic basalt and evaluation of pre-eruptive processes, *J. Petrol., 47*, 883-900.

1307 Roult, G., A. Peltier, T. Staudacher, V. Ferrazzini, B. Taisne, A. Di Muro, and The OVPF
1308 Team (2012), A comprehensive classification of the Piton de la Fournaise eruptions (La
1309 Réunion Island) spanning the 1986–2010 period. Search for eruption precursors from the

1310 broad-band GEOSCOPE RER station analysis and interpretation in terms of volcanic
1311 processes, *J. Volcanol. Geotherm. Res., 241*, 78–104.

1312 Rust, A.C., and K.V. Cashman (2011), Permeability controls on expansion and size
1313 distributions of pyroclasts, *J. Geophys. Res., 116*, B11202.

1314 Saar, M.O., M. Manga, K.V. Cashman, and S. Fremouw (2001) Numerical models of the
1315 onset of yield strength in crystal-melt suspensions: *Earth Planet. Sci. Lett., 187*, 367–379, doi:
1316 10 .1016 /S0012 -821X (01)00289 -8.

1317 Salaün, A., Villemant, B., Semet, M.P., and T. Staudacher (2010), Cannibalism of olivine-rich
1318 cumulate xenoliths during the 1998 eruption of Piton de la Fournaise (La Réunion hotspot):
1319 Implications for the generation of magma diversity. *J.Volcanol. Geother. Res., 198*, 187-204.

1320 Schiano, P., K. David, I. Vlastélic, A. Gannoun, M. Klein, F. Nauret, and Bonnand P. (2012),
1321 Osmium isotope systematics of historical lavas from Piton de la Fournaise (Réunion Island,
1322 Indian Ocean), *Contrib. Mineral. Petrol.,* http://dx.doi.org/10.1007/s00410-012-0774-0.

1323 Shea, T., (2017) Bubble nucleation in magmas: a dominantly heterogeneous process? *J.*
1324 *Volcanol. Geotherm. Res. 343,* 155–170.

1325 Shea, T., B.F. Houghton, L. Gurioli, K.V. Cashman, J.E. Hammer, and B. Hobden (2010),
1326 Textural studies of vesicles in volcanic rocks: an integrated methodology, *J. Volcanol.*
1327 *Geotherm. Res., 190*, 271–289.

1328 Shea, T., L. Gurioli, and B.F. Houghton (2012), Transitions between fall phases and
1329 pyroclastic density currents during the AD 79 eruption at Vesuvius: building a transient
1330 conduit model from the textural and volatile record, *Bull. Volcanol., 74*, 2363–2381,
1331 doi:10.1007/s00445-012-0668-z.

1332 Sparks, R.S.J. (1978), The dynamics of bubble formation and growth in magmas: a review
1333 and analysis, *J. Volcanol. Geotherm. Res., 3*, 1–37.

1334 Sparks, R.S.J. (2003). Forecasting volcanic eruptions, *Earth Planet. Sci. Lett., 210*, 1–15.

1335 Spina, L., C. Cimarelli, B. Scheu, D. Di Genova, and D. B. Dingwell (2016) On the slow
1336 decompressive response of volatile- and crystal-bearing magmas: An analogue experimental
1337 investigation, *Earth Planet. Sci. Lett., 433*, 44-53.

Staudacher, T., and A. Peltier (2015), Ground deformation at Piton de la Fournaise (La Réunion Island), a review from 20 years of GNSS monitoring, In: Bachèlery P, Lénat, JF, Di Muro A, Michon L (ed) Active volcanoes of the Southwest Indian Ocean: Piton de la Fournaise and Karthala. Active volcanoes of the world. Springer, Berlin, 139-170. doi:10.1007/978-3-642-31395-0_9

Staudacher, T., V. Ferrazzini, A. Peltier, P. Kowalski, P. Boissier, P. Catherine, F. Lauret, and F. Massin (2009), The April 2007 eruption and the Dolomieu crater collapse, two major events at Piton de la Fournaise (La Re¤union Island, Indian Ocean). *J. Volcanol. Geother. Res. 184*, 126-137, doi:10.1016/j.jvolgeores.2008.11.005.

Stovall, W.K., B.F. Houghton, H.M. Gonnermann, S.A. Fagents, and D.A. Swanson (2011), Eruption dynamics of Hawaiian-style fountains: the case study of episode 1 of the Kīlauea Iki 1959 eruption, *Bull. Volcanol. 73*, 511–529. doi:10.1007/s00445-010-0426-z.

Stovall, W.K., B.F. Houghton, J.E. Hammer, S.A. Fagents, and D.A. Swanson (2012), Vesiculation of high fountaining Hawaiian eruptions: episodes 15 and 16 of 1959 Kīlauea Iki, *Bull. Volcanol., 74*, 441–455, doi:10.1007/s00445-011-0531-7.

Swanson, D.A., K. Wooten, and T. Orr (2009), Buckets of ash track tephra flux from Halema'uma'u crater, Hawai'i. *Eos Trans. AGU, 90*, 427–428. doi:10.1029/2009EO460003. Taddeucci, J., M. Pompilio, and P. Scarlato (2002), Monitoring the explosive activity of the July–August 2001 eruption of Mt. Etna (Italy) by ash characterization, *Geophys. Res. Lett., 29*(8), 1029–1032. doi:10. 1029/2001GL014372.

Tait, S., C. Jaupart, and S. Vergniolle (1989), Pressure, gas content and eruption periodicity of a shallow, crystallising magma chamber, *Earth Planet. Sci. Lett., 92*, 107-123.

Takeuchi, S., S. Nakashima, and A. Akihiko Tomiya (2008) Permeability measurements of natural and experimental volcanic materials with a simple permeameter: toward an understanding of magmatic degassing processes, *J. Volcanol. Geotherm. Res.*, 177:329–339.

Thornber, C.R., K. Hon, C. Heliker, and D.A. Sherrod (2003), A Compilation of Whole-Rock and Glass Major-Element geochemistry of Kīlauea Volcano, Hawai'i, near-vent eruptive products: January 1983 through September 2001: *U.S.G.S. Open File Report*, *03*-477.

1366 Thordarson, T, S Self, N Óskarsson, and T Hulsebosch (1996), Sulfur, chlorine and fluorine
1367 degassing and atmospheric loading by the 1783–1784 AD Laki (Skaftár Fires) eruption in
1368 Iceland, *Bull. Volcanol. 58*, 205–225.

1369 Villemant, B., A. Salaün, and T. Staudacher (2009), Evidence for a homogeneous primary
1370 magma at Piton de la Fournaise (La Réunion): A geochemical study of matrix glass, melt
1371 inclusions and Pélé's hairs of the 1998–2008 eruptive activity, *J. Volcanol. Geotherm. Res.,*
1372 *184*, 79–92.

1373 Vlastélic, I., and A.J. Pietruszka (2016), A review of the recent geochemical evolution of
1374 Piton de la Fournaise Volcano (1927–2010). In: Bachèlery, P., Lénat, J.F., Di Muro, A.,
1375 Michon, L. (Eds.), Active Volcanoes of the Southwest Indian Ocean. In: Active Volcanoes of
1376 the World, pp.185–201.

1377 Vlastélic, I., A. Peltier, and T. Staudacher (2007), Short-term (1998-2006) fluctuations of Pb
1378 isotopes at Piton de la Fournaise volcano (Réunion Island): origins and constraints on the size
1379 and shape of the magma reservoir, *Chem. Geology, 244*, 202-220.

1380 Vlastélic, I., C. Deniel, C. Bosq, P. Telouk, P. Boivin, P. Bachèlery, V. Famin,. and T.
1381 Staudacher (2009), Pb isotope geochemistry of Piton de la Fournaise historical lavas, *J.*
1382 *Volcanol. Geother. Res., 184*, 63-78.

1383 Vlastélic, I., T. Staudacher, P. Bachèlery, P. Télouk, D. Neuville., and M. Benbakkar (2011)
1384 Lithium isotope fractionation during magma degassing: constraints from silicic differentiates
1385 and natural gas condensates from Piton de la Fournaise volcano (Réunion Island), *Chemical*
1386 *Geology, 284*, 26–34.

1387 Vlastélic, I., G. Menard, M. Gannoun, J.-L Piro., T Staudacher, and V. Famin (2013), Magma
1388 degassing during the April 2007 collapse of Piton de la Fournaise: the record of semi-volatile
1389 trace elements (Li, B, Cu, In, Sn, Cd, Re, Tl, Bi), *J. Volcanol. Geother. Res., 254*, 94-107.

1390 Vlastélic, I., A. Gannoun, A. Di Muro, L. Gurioli, P. Bachèlery, and J.M. Henot (2016), Origin
1391 and fate of sulfide liquids in hotspot volcanism (La Réunion): Pb isotope constraints from
1392 residual Fe–Cu oxides, *Geochim. Cosmochim. Acta, 194*, 179-192.

1393 Welsch, B., F. Faure, P. Bachèlery, and V. Famin (2009), Microcrysts record transient
1394 convection at Piton de la Fournaise volcano (La Réunion Hotspot), *J. Petrol., 50*, 2287-2305.

1395 Welsch, B., V. Famin, A. Baronnet, and P. Bachèlery (2013), Dendritic crystallization: a single

1396 process for all textures of olivine in basalts? *J. Petrol., 54*, 539-574.

1397 White, J.D.L., and B.F. Houghton (2006), Primary volcaniclastic rocks, *Geology, 34*, 677–

1398 680, doi:10.1130/G22346.1.

1399
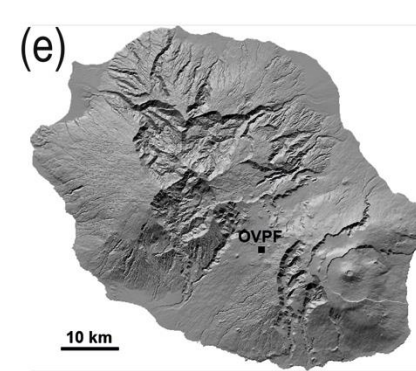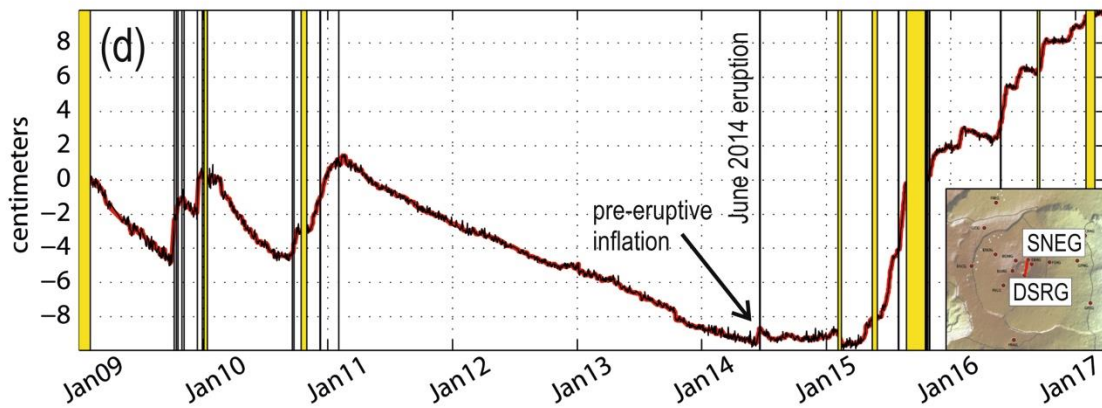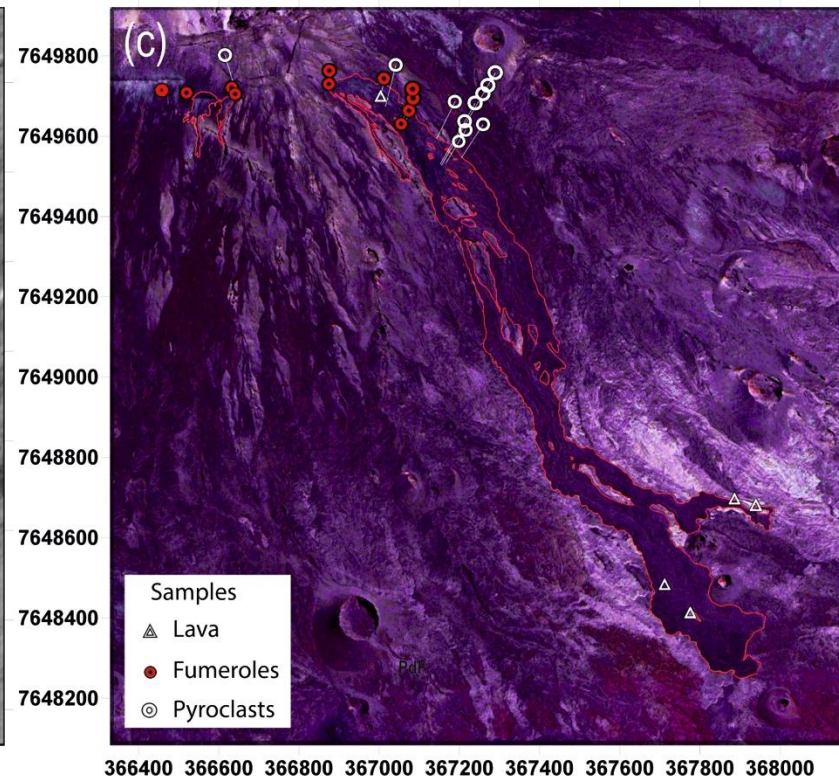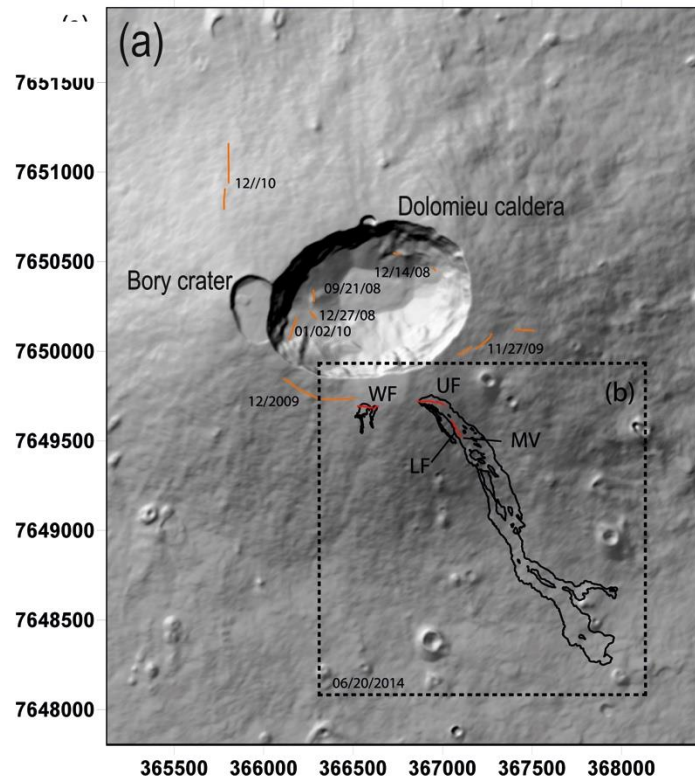
Figure 1 a) Digital elevation model of the summit crater area at Piton de la Fournaise, La Réunion, France; orange = fractures generated by pre-2014 eruptions (reported are the dates of their activities); b) red = fractures active during the 2014 eruption: WF (Western Fracture), UF (Upper Fracture), LF (Lower Fracture), MV (Main Vent). Black= outline of the 2014 lava field; c) locations of sample collection points. The coordinates are in UTM, zone 40 south. (d) Distance change (baseline) in centimetres between two GNSS summit stations: DSRG and SNEG (see location in the inset). Increase and decrease of the signal mean a summit inflation and deflation, respectively. The yellow areas represent eruptive and intrusive periods. In Figure 1d, the rapid and strong variations linked to dike injections preceding intrusions and eruptions by a few tens of minutes have been removed; (e) Digital Elevation Model of La Réunion island.

47

June 2014 eruption at PdF

Early morning, June 21

a)

b)

June 21 ~ 7h00

c)

June 21, 7h38

d)

June 21, 13h35

e)

June 21,17h00

f)

g)

1410

Figure 2 Photos collection from the 2014 eruption at the MV, highlighted with a white cross (see location in Fig. 1). From a to g: evolution of the Strombolian activity from early morning to evening, June 21 that shows a decline in the activity with time. Unfortunately, the relatively more energetic Hawaiian fountaining events that happened during the night were not documented. a) Strombolian activity at the MV and associated lava flow; b) zoom view of the Strombolian activity at the MV. The images in a, b and the inset in b are from Laurent Perrier; c) aerial view of the SE flank of the PdF, taken by the OVPF team from the helicopter of the gendarmerie of La Réunion; d) Eastern front of the lava where the OVPF team collected a quenched lava sample; e) low Strombolian activity at the MV and the associated lava flow, photo from: http://www.ipreunion.com/volcan/reportage/2014/06/21/eruption-du-piton-de-la-fournaise-actualise-a-17h-la-lave-coule-sur-1-5-kilometre,26023.html; f) and g) decline of the Strombolian activity at the MV, the photo in e) is from http://www.zinfos974.com/L-eruption-du-Piton-de-la-Fournaise-Le-point-de 17h_a72981.html; and the photo if f) is from: f) http://nancyroc.com/eruption-a-la-reunion

49

Main Vent
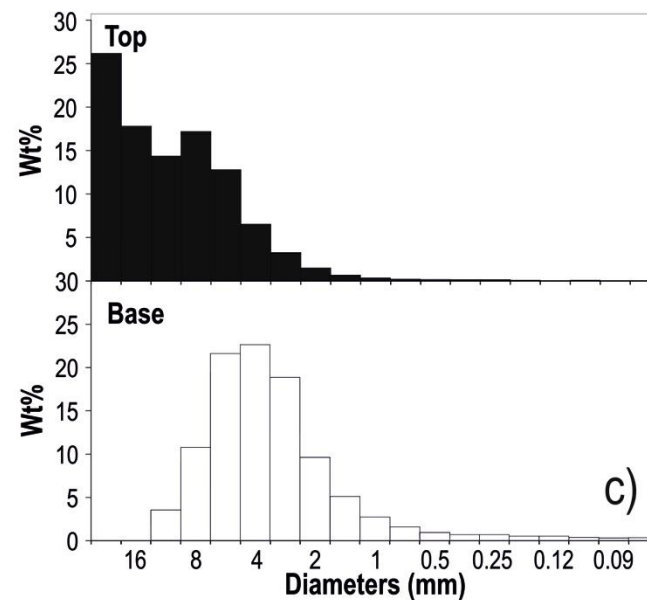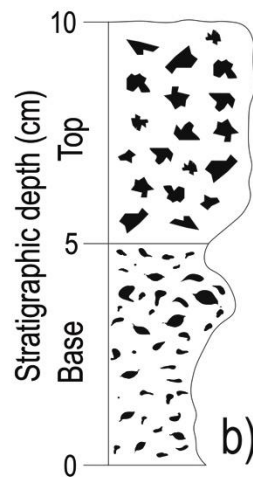
Western fracture
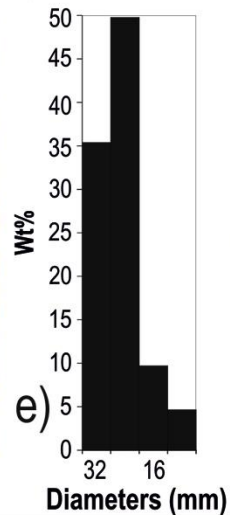
2010 Fountaining

2014 Explosions
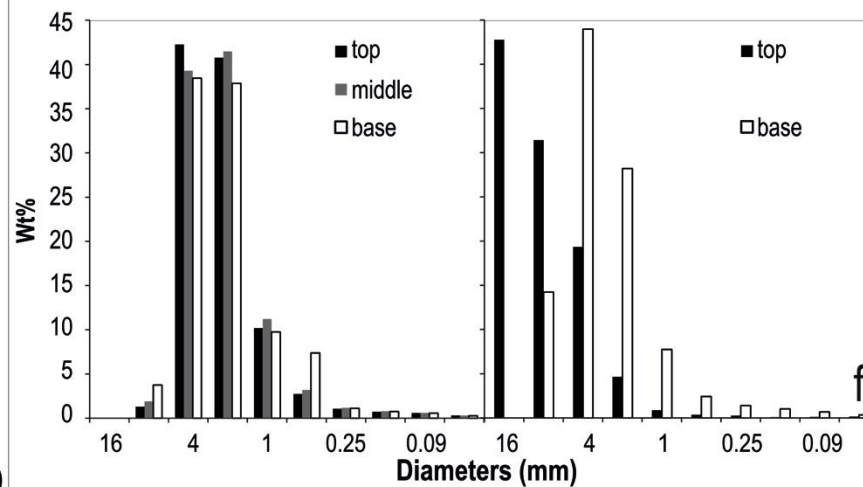
1438 **Figure 3** a) Continuous blanket of scoria fall out deposit emitted from the MV (Fig. 1 for location) during June 2014 eruption at PdF. The black

1439 cross locates the position of the MV (see Fig. 1 for the location); b) schematic stratigraphic log of the scoria fall out deposit emplaced during

1440 June 2014 eruption at the MV. c) grain size histograms of the base and the top of the deposit of the MV, the particle diameters are at half phi; d)

1441 scattered scoria (outlined in yellow) from the WF (see Fig. 1 for the location); e) grain size histogram of the scoria deposit at the WF, the particle

1442 diameters are at half phi; f) comparison between the grain size histograms for the 2010 Hawaiian fountaining and the 2014 MV activity, both the

1443 particle axes are reported in full phi for comparison.

1444

1445

1446

1447

1448
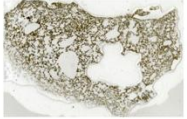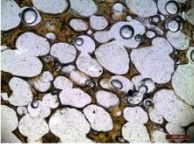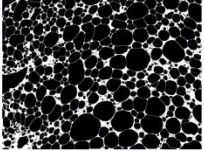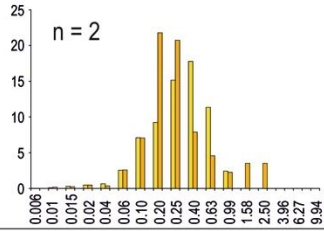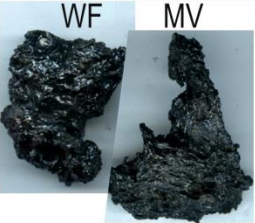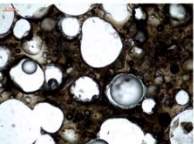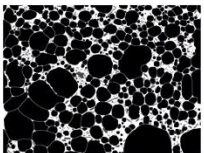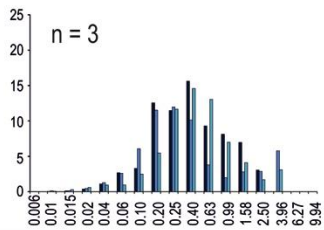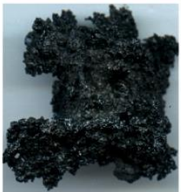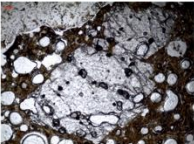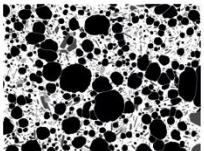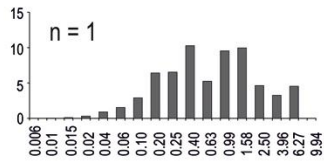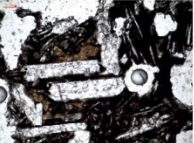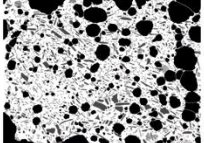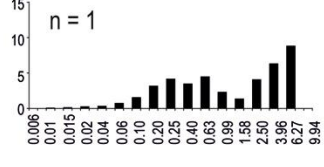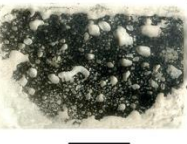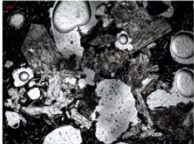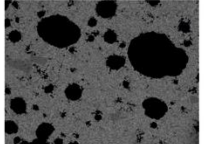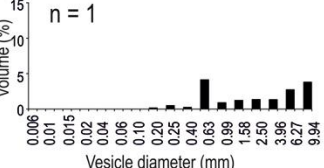
1449

1450

1451

1452

1453

Type	Clast	Thin section	Microscope	SEM (25X)	VSD	Crystal vol %	N_v
Golden Pumice (a)			0.02 mm		n = 2	Tot = 8-15 Mplg= rare µplg = 6-11 Mcpx = rare µcpx =(1-3)	2×10^7 9×10^6
Fluidal Scoria (b)	WF MV		0.02 mm		n = 3	Tot = 4-23 Mplg = 0.4-1 µplg = 2-19 Mcpx = 0-1 µcpx = 1-4	2×10^7 5×10^6 3×10^6
Spiny glassy scoria (c)			0.02 mm		n = 1	Tot = 51 Mplg = 11 µplg = 23 Mcpx =15 µcpx = 2	6×10^6
Spiny opaque scoria (d)	1 cm				n = 1	Tot = 55 Mplg = 11 µplg = 25 Mcpx = 10 µcpx = 9	4×10^6
Lava (e)	1m	1 cm	0.02 mm	1 mm	n = 1 Volume (%) Vesicle diameter (mm)	Tot = 100 Mplg = 2 µplg = 64 Mcpx = 3 µcpx = 31	2×10^4

1454

52

1455 **Figure 4** Textural features of June 2014 pyroclasts and lava. Clast = photo of the different types of juvenile pyroclasts and lava channel. The

1456 photo of the lava channel is from Laurent Perrier. WF = Western Fracture (smooth fluidal scoria), MV = Main Vent (fluidal scoria, less smooth

1457 than the ones at the WF). Thin section = thin section imaged with a desktop scanner. Microscope = picture taken with an optical microscope

1458 using natural light; SEM (25X) = image captured using a scanning electron microscopy (SEM), in BSE mode at 25x magnification: black are

1459 vesicles, white is glass, grey are crystals. VSD = vesicle size distribution histograms, where the diameter, in mm, is plotted versus the volume

1460 percentage, n = number of measured clasts; Crystal vol. % : Tot = total percentage of crystals corrected for the vesicularity; Mplg = percentage

1461 of mesocrysts of plagioclase; μplg = percentage of microcrysts of plagioclase; Mcpx = percentage of mesocrysts of pyroxene; μcpx = percentage

1462 of microcrysts of pyroxene; Nv = number density corrected for the vesicularity.

1463

1464
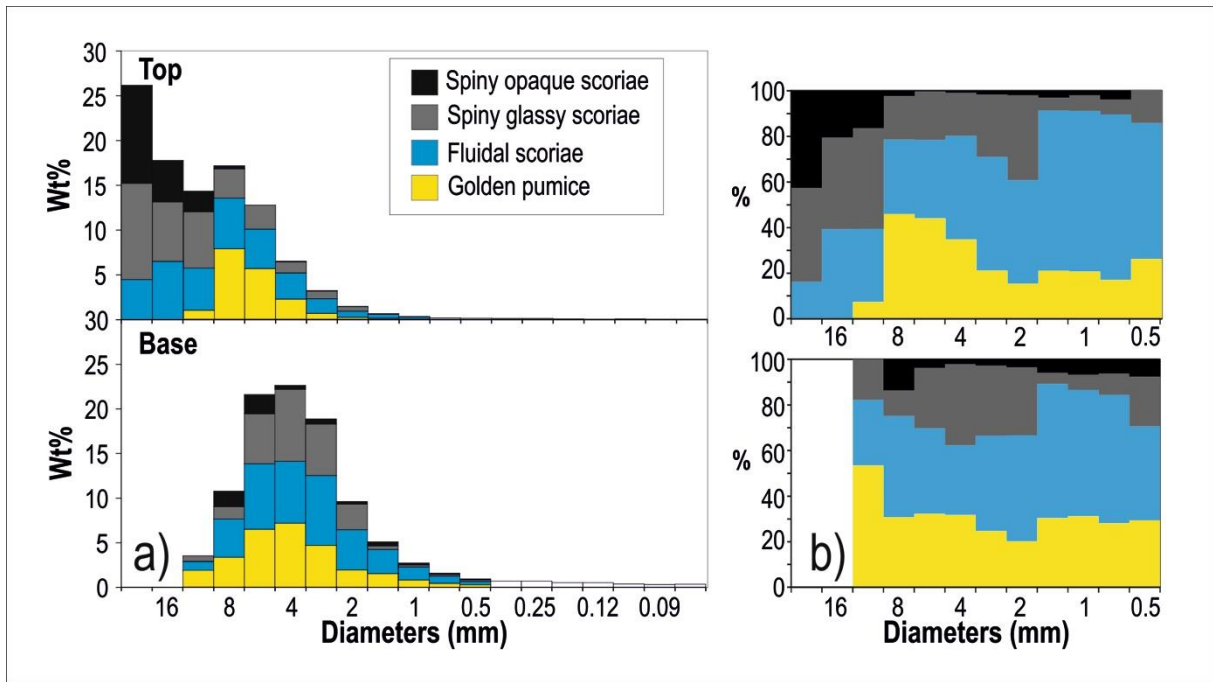
1467 **Figure 5** Proportion of each type of clast measured from the base to the top of the 10 cm thick
1468 deposit emplaced during the eruption, at the MV site. The deposit is dominated by Hawaiian-
1469 like lapilli fragments at the base (golden pumice and fluidal scoria) and Strombolian-like
1470 bombs and lapilli at the top (spiny scoria): (a) componentry within the different grain size
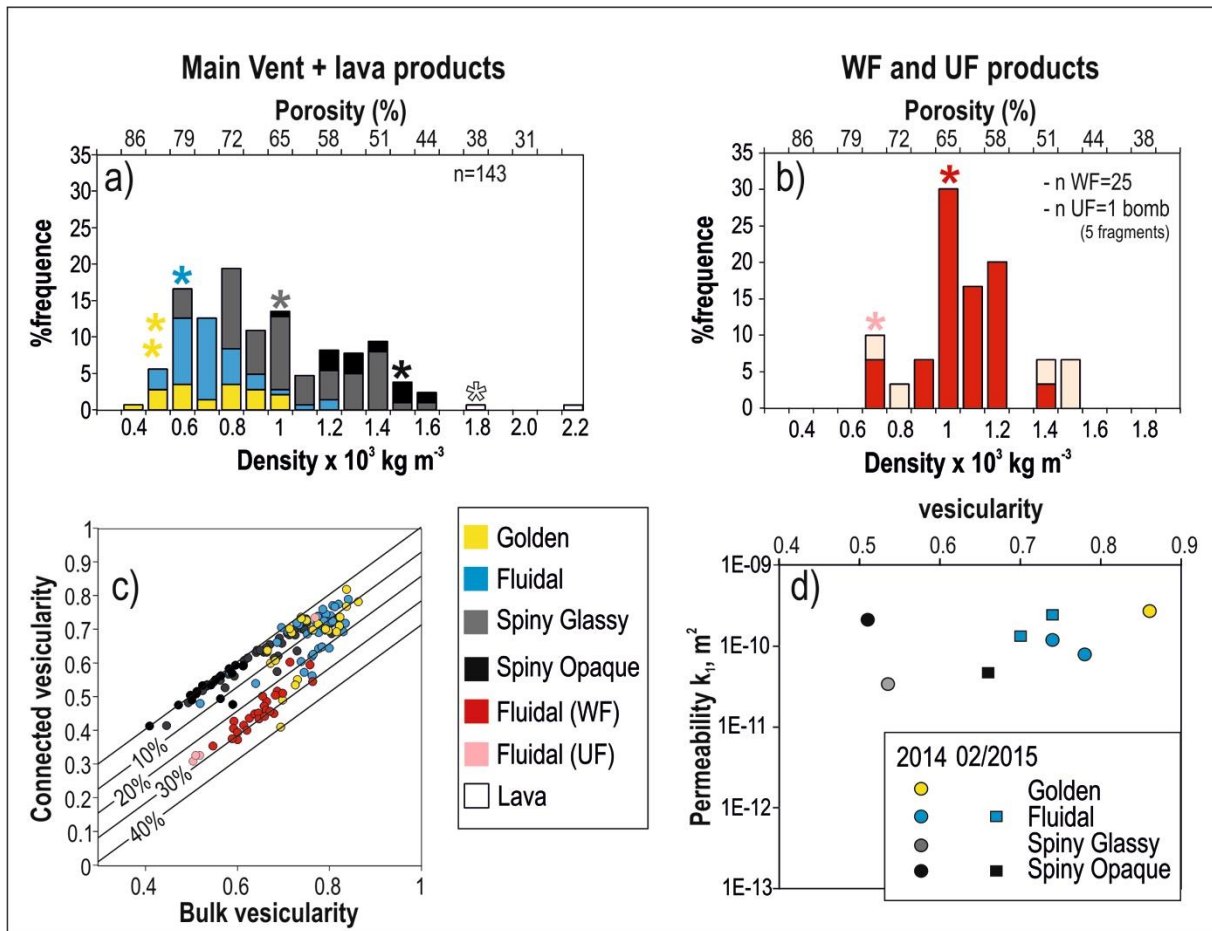1471 classes; b) normalized componentry composition from the base to the top of the deposit.

1472

1473

1474

1475

1476

1477

1478

1479

1480

Figure 6 Density, connectivity and permeability data of June 2014 pyroclast and lava fragments: a) density distribution histogram for all the pyroclast fragments measured at the MV + two lava fragments collected from the Eastern front of the lava flow (see Fig. 1 for location). n = number of measured clasts; b) density distribution histogram for the pyroclasts sampled at the WF and the bomb sampled at the UF. The bomb broke in five fragments (2 fragments from the core, the least dense, and three fragments from the quenched edges, the densest). In both the density histograms the stars represent the density intervals from which we picked the clasts for the textural measurements; c) graph of the connected vesicularity versus total vesicularity. The diagonal line represents equality between the connectivity and vesicularity, beneath this line the samples have isolated vesicles and the straight lines represent lines of equal fraction of isolated vesicles. To note that the bomb from the UF has the high vesicular core with less than 5% of isolated vesicles, while the three low vesicular fragments from the quenched edge have more than 25% of isolated vesicles (see pink spots); d) Darcian viscous permeability (k_1) versus vesicularity fraction for the four typologies of clasts collected at the MV. For comparison, two fluidal fragments and one spiny opaque fragments from February 2015 eruption are reported.

55
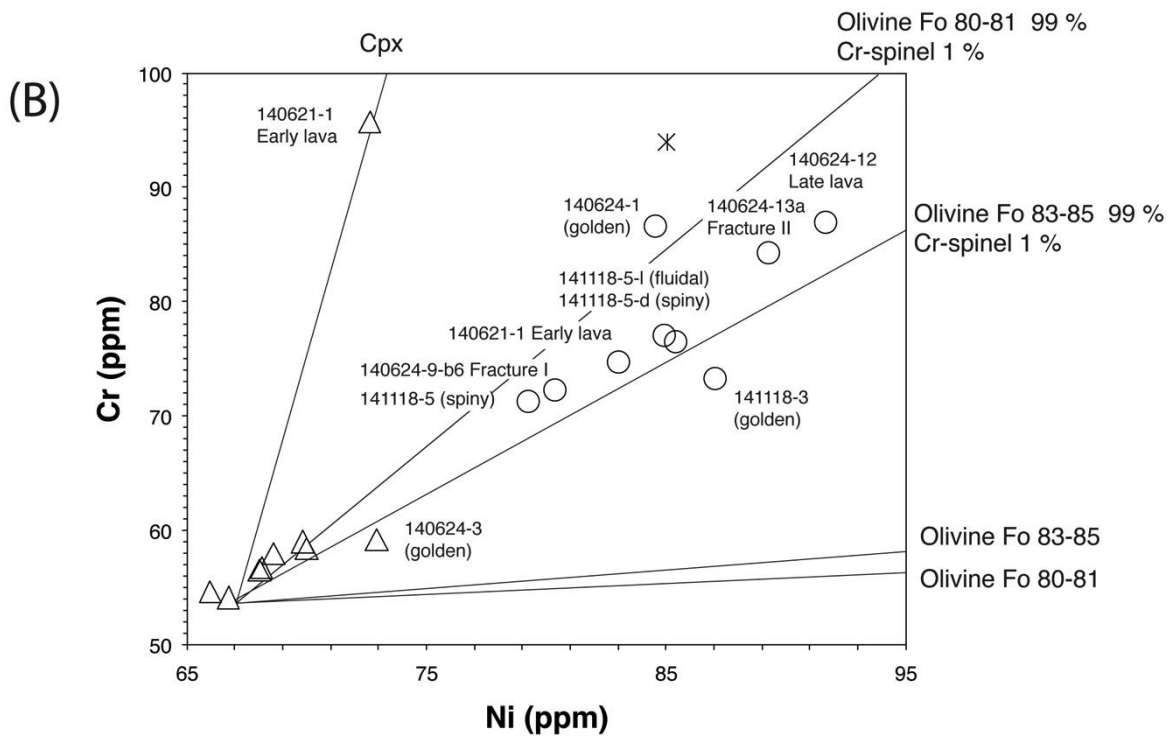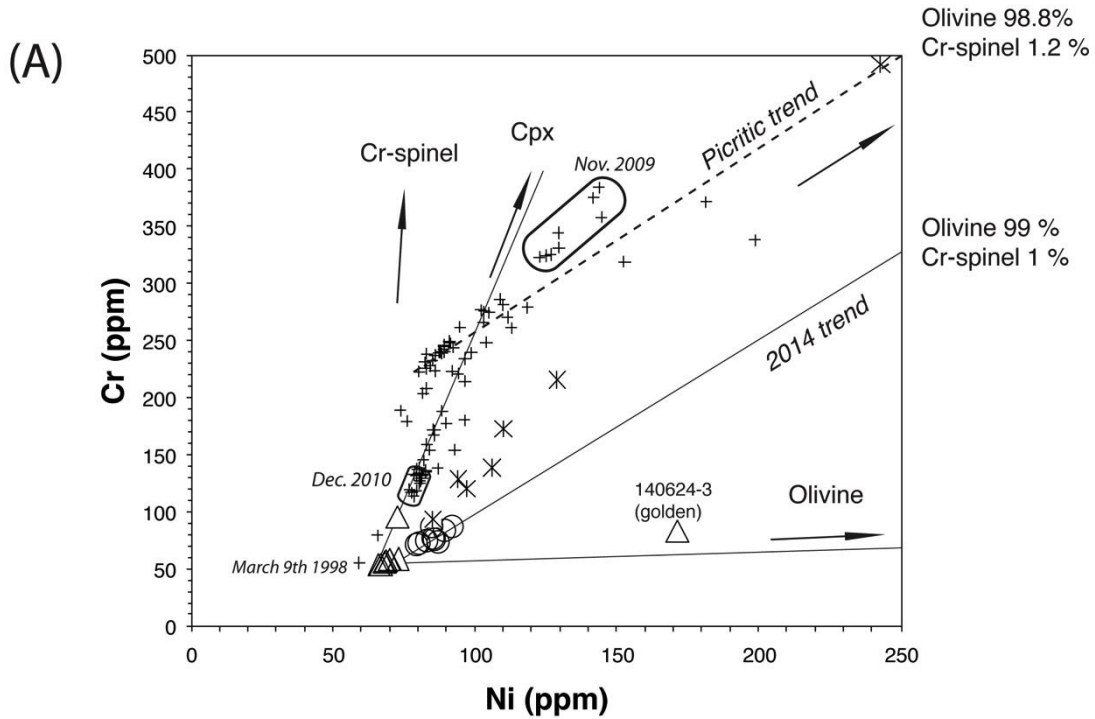
Figure 7 Ni-Cr concentration plot. (a) Ni-Cr signature of the June 2014 lavas compared to that of recent eruptions (Di Muro et al. (2015) and unpublished data). Whole-rock (circles) and glass (triangles) compositions are shown for the June 2014 eruption. Olivine controlled lines are indicated for olivine hosting 1.2 and 0.6 wt.% Cr-spinel. Compositions used for olivine (Ni=1900 ppm, Cr=300ppm), clinopyroxene (Ni=970 ppm, Cr=4800 ppm), and Cr spinel (Ni=1500 ppm, Cr=25%) are inferred from Welsch et al. (2009), Salaün et al. (2010), and Di Muro et al. (2015). (b) Zoom of the Ni-Cr relationship between glass (triangles) and whole-rock (circles) samples from the June 2014 eruption. Fracture I = Western Fracture, Fracture II = Upper Fracture. Careful sample selection has permitted to obtain a set of virtually olivine-cpx free crystals. Any addition of mafic crystals translates into enrichment in Ni-Cr; those samples that contain a few % of crystals (consistent with textural and petrological observation) are slightly enriched in compatible elements.

57
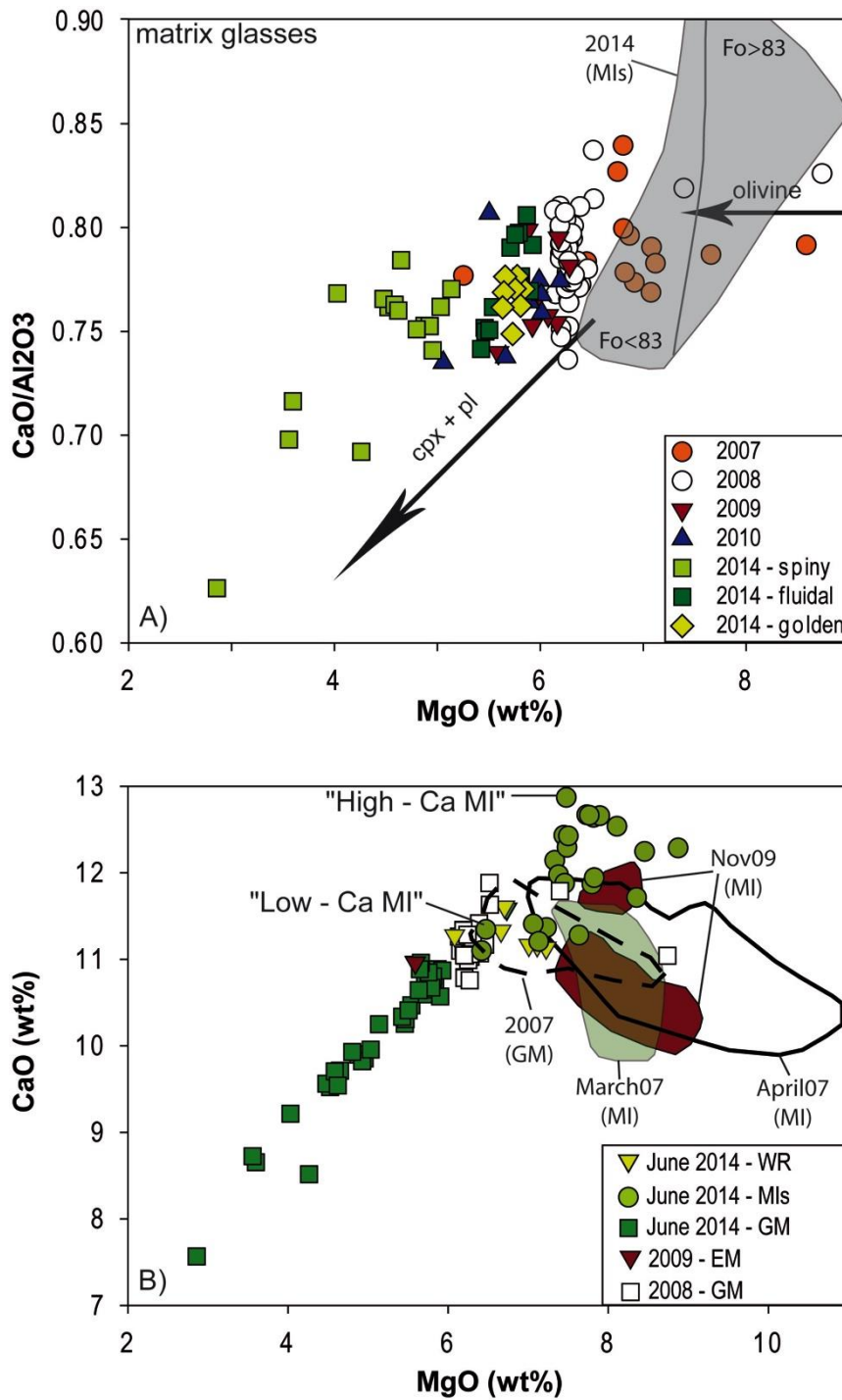
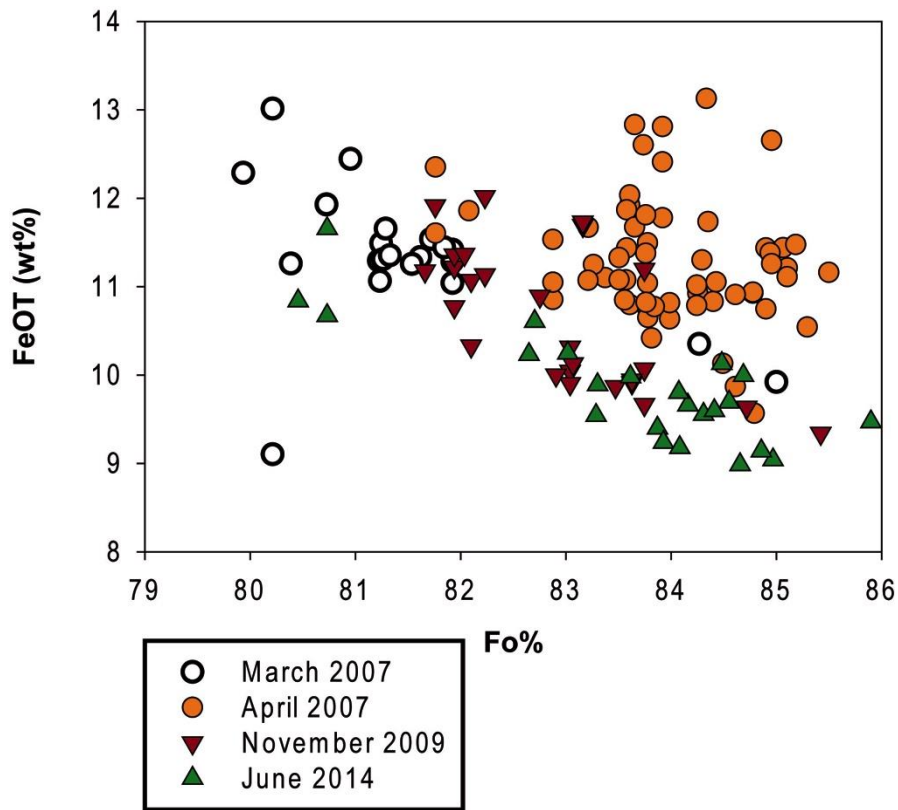Fig. 8 (a) Evolution of CaO/Al$_2$O$_3$ ratio in the matrix glasses of recent eruptions at Piton de la Fournaise as a function of MgO content (directly proportional to melt temperature). MI = Melt inclusions (grey area for the 2014 samples). (b) CaO versus MgO content for Piton de la Fournaise products. WR = whole rock, GM = ground mass; MI = melt inclusion, EM = embayment glass

1521

1522 **Figure 9** FeO_T in melt inclusions as function of Fo content of the olivine host for recent
1523 eruptions at Piton de la Fournaise

1524

1525

1526

1527

1528

1529

1530

1531

1532

1533

1534
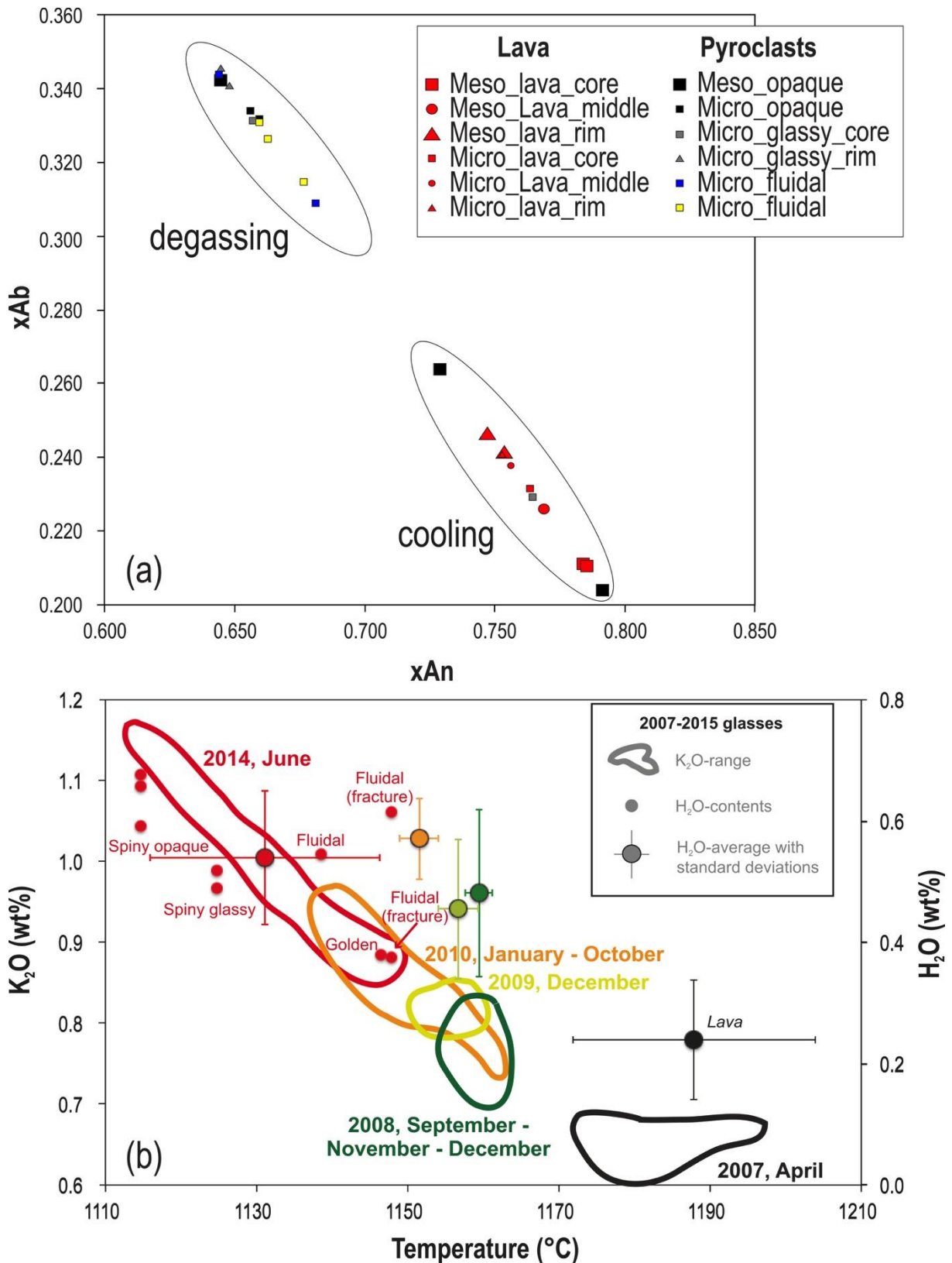
Figure 10 a) Anorthite versus Albite compositions for the plagioclase crystals measured for June 2014 eruption of PdF; b) Temperature, composition (K_2O) and dissolved water content (H_2O) for the evolution of 2007-2014 melts from glasses. The data have been obtained by

60

studying the glass-plagioclase equilibrium or on the basis of matrix glass analyses. Temperature estimation based on the MgO-thermometer of Helz and Thornber (1987) modified by Putirka (2008). Water content is from the plagioclase hygrometer of Lange et al. (2009). Only plagioclases in equilibrium with melts are considered, following the procedure described by Putirka (2008) for >1050°C melts (Kd = 0.27±0.05). Error bars reported in Figure 10b correspond to the standard deviation of the plagioclase dataset, whose range is larger than error of the method. We stress that the reported temperatures are obtained using Helz dry model. Further uncertainty arises from the dependence of the method on dissolved water content as shown recently by Putirka (2008). In order to minimize the number of assumptions and perform a comparison between distinct eruptions, we preferred to adopt the dry model.
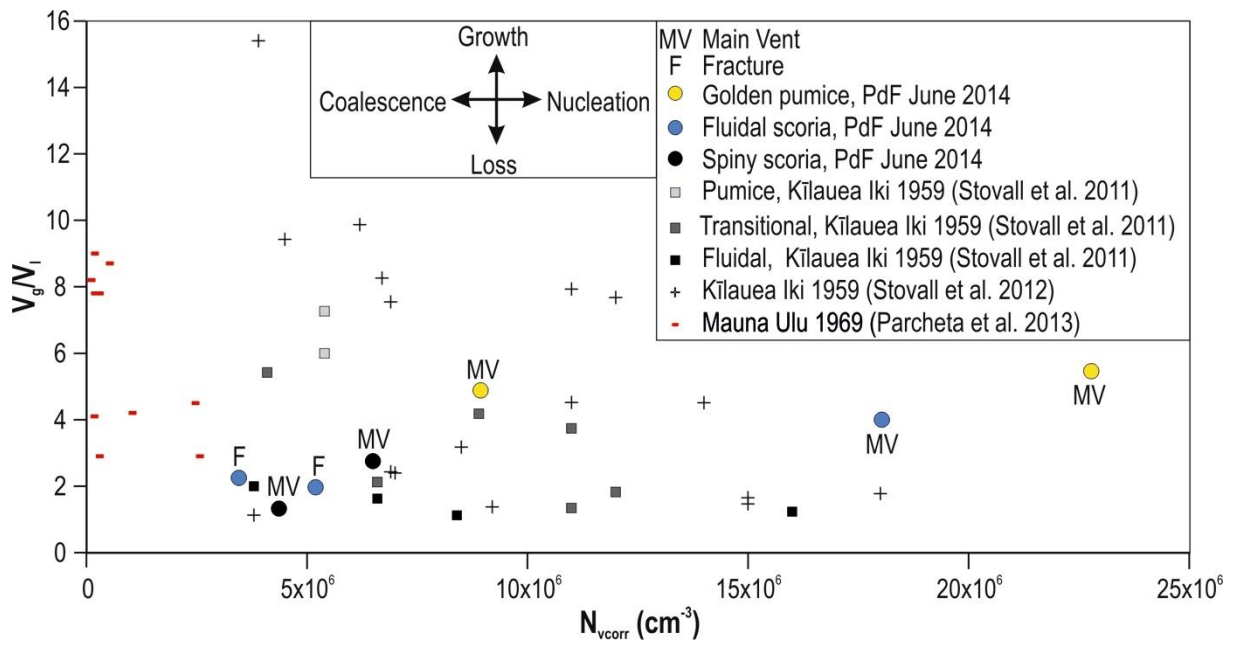
1571

Figure 11 Volumetric ratio of vesicles to melt (V_G/V_L) versus vesicle number density

1573
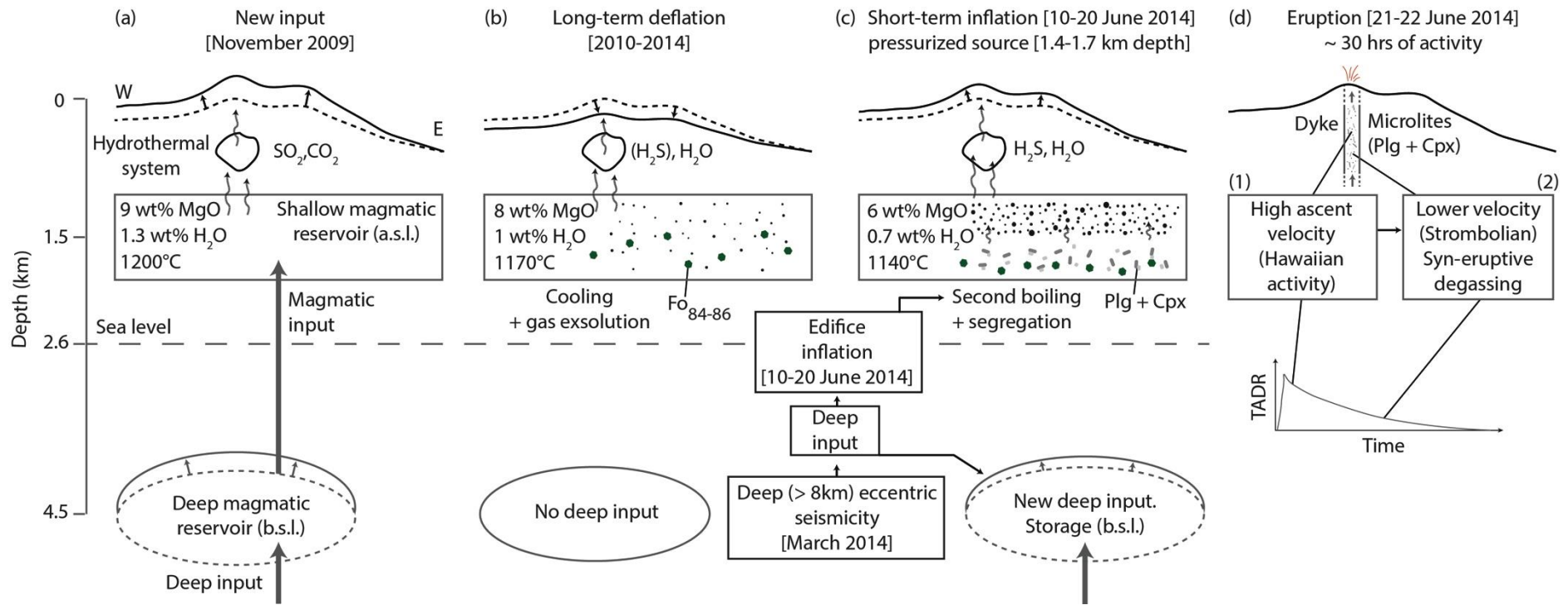
1574

1575   **Figure 12** Schematic model of the evolution of PdF volcanic system from the new deep magmatic input of November 2009 up to June 2014

1576   eruption. See explanation in the text